Cenozoic lateritic weathering and erosion history of Peninsular India from 40 Ar/ 39 Ar dating of supergene K-Mn oxides

Nicolas J Bonnet, Anicet Beauvais, Nicolas Olivier Arnaud, Dominique Chardon, Mudlappa J Jayananda

Cenozoic lateritic weathering and erosion history of Peninsular India from $^{40}Ar/^{39}Ar$ dating of supergene K-Mn oxides

Nicolas J. Bonnet [1*], Anicet Beauvais [1*], Nicolas Arnaud [2], Dominique Chardon [3,4,5], Mudlappa Jayananda [6]

[1] Aix-Marseille Université (AMU), IRD (Institut de Recherche pour le Développement), CNRS (Centre National de la Recherche Scientifique), CEREGE (Centre Européen de Recherche et d'Enseignement des Géosciences de l'Environnement) UM34, BP 80, 13545 Aix-en-Provence, Cedex 4, France

[2] Université de Montpellier 2, Géosciences Montpellier, UMR CNRS 5243, 34095 Montpellier, France

[3] IRD, UMR 234, GET, 14 Avenue Edouard Belin, 31400 Toulouse, France

[4] Université de Toulouse, UPS (Université Paul Sabatier) OMP (Observatoire Midi-Pyrénées), 31400 Toulouse, France

[5] CNRS, GET, 31400 Toulouse, France

[6] Centre for Earth and Space Sciences, University of Hyderabad, P.O Central University Gachibowli, Hyderabad 500 046, India

Submitted to Chemical Geology, October 7th 2015

Revised, April 15, 2016
Accepted April 20, 2016

*Correspondings authors: nicolas.bonnet.geo@gmail.com; beauvais@cerege.fr

Abstract

Since Deccan Traps extrusion ~ 65 Ma ago, thick weathering mantles have developed over Peninsular India on both the western coastal lowland and adjacent plateau separated by the Western Ghats Escarpment. Manganiferous lateritic profiles formed by supergene weathering of Late Archean manganiferous protores are exposed on paleolandsurface remnants on both sides of the escarpment. Petrological and geochemical characterizations of samples from those Mn lateritic profiles allowed identifying cryptomelane (K-Mn oxide) dated by $^{40}Ar/^{39}Ar$ geochronology. The ages obtained document major weathering periods, ca. 53-50 Ma, and ca. 37-23 Ma in the highland, and ca. 47-45 Ma, ca. 24-19 Ma and discrete weathering pulses at ~ 9 Ma and ~ 2.5 Ma in the lowland. Old ages of the highland (53-50 Ma) and the lowland (47-45 Ma) indicate synchronous lateritic weathering across the escarpment at a time the peninsula started to drift across the equatorial belt. Intense weathering periods at ca. 53-45 and ca. 37-23 Ma are interpreted to reflect the Early Eocene climatic optimum and the onset of Asian monsoon regimes, respectively. The ages further indicate that most of the dissection of the highland must have taken place after ~ 23 Ma, whereas the lowland was weakly incised essentially after ~ 19 Ma. Our results also document divergent erosion and weathering histories of the lowland and the highland after the Eocene, suggesting installation of a dual climatic regime across the Western Ghats escarpment.

Keywords: $^{40}Ar/^{39}Ar$ geochronology; Supergene Mn-oxides; Mn-ore deposits; Lateritic weathering; Cenozoic; India

1. Introduction

Chemical rock weathering that results in the accumulation of metals such as Al, Fe or Mn, and relative depletion of silica and base elements, produce lateritic regoliths covering shields in the tropical belt. Weathering processes are intense under wet and warm climate that characterizes most tropical forest's soil environments (Pedro, 1968; Ollier, 1988; Nahon, 1991; Tardy, 1997). Metals are mostly retained in duricrusts capping thick weathering profiles, which are, in turn, partly preserved from mechanical erosion. Therefore, old lateritic weathering profiles several tens of meters thick may be preserved on paleolandsurface remnants for several millions years (Bárdossy and Aleva, 1990; Thomas, 1994; Tardy and Roquin, 1998; Valeton, 1999; see also Beauvais and Chardon, 2013).

Since Deccan Traps extrusion ~ 65 Ma ago, the surface of the Indian peninsula was shaped by combined or alternating chemical weathering and mechanical erosion processes that resulted in composite landscapes made of stepped lateritic paleolandsurfaces remnants of various generations occurring on either side of the Western Ghats Escarpment (WGE) (e.g., Widdowson, 1997; Gunnell, 1998). This escarpment was carved both into Deccan Traps and Precambrian basement rocks and separates a western lowland from a dissected hinterland also known as the Mysore plateau (Radhakrishna, 1993; Gunnell, 1998; Widdowson and Gunnell, 1999).

Time constraints on the formation of South Indian laterites are still poorly documented (Schmidt et al., 1983; Krishna Rao et al., 1989a) although Late Paleogene $^{40}Ar/^{39}Ar$ ages of supergene K-Mn oxides have been recently obtained from the Sandur Mn-ore deposit on the highland (Bonnet et al., 2014). Most south Indian Mn-ore deposits result from supergene weathering of late Archean supracrustal rocks, either on the highland in the Sandur and Shimoga areas (Krishna Rao et al., 1982; Mohapatra et al., 1996), or in the lowland at the foot of the WGE (Dessai, 1985; Fig. 1). In both contexts, Mn-ore deposits are hosted by lateritic weathering profiles underlying remnants of several generations of paleosurfaces, which are preserved at variable elevations (Fig. 2). All these Mn-ore deposits contain K-rich Mn oxides such as cryptomelane [$K_x\ Mn_{8-x}^{IV}\ Mn_x^{III}\ O_{16}$], which is datable by $^{40}Ar/^{39}Ar$ geochronology. Absolute dating of K-Mn oxides generally documents periods of intense lateritic weathering controlled by specific paleoclimatic conditions and as such may be used to reconstruct and quantify the long-term morphoclimatic evolution of tropical shield surfaces (Beauvais et al., 2008; Beauvais and Chardon, 2013; Vasconcelos, 1999b; Vasconcelos and Conroy, 2003). Here we report on $^{40}Ar/^{39}Ar$ geochronological data series obtained on Peninsular India that bracket three Cenozoic weathering periods and constrain the tempo of long-term South Indian morphogenesis. Our results also document divergent erosion and weathering histories across the WGE suggesting installation of a dual climatic regime on either side of the escarpment after the Eocene warming period.

2. Material and methods

2.1. Geological and geomorphological setting

South Indian laterites have been discriminated in two groups: highland laterites on the plateau and lowland laterites in the western coastal plain (e.g., Widdowson and Cox, 1996). Remnants of three main lateritic paleolandsurfaces are reported on the highland and the remnants of a lateritic pediment have been described in the lowland (Widdowson, 1997; Gunnell, 1998; Widdowson and Gunnell, 1999). Our field observations indicate that each highland relict paleolandsurface has a specific regolith covers. The relicts of the first, highest and oldest landsurface are capped by a weathering profile topped by an Al-Fe duricrust (Figs. 2). This duricrust is commonly economic-grade bauxite such as those preserved on the Deccan Traps (Valeton, 1999). The bauxites are also preserved on the highest topographic massifs of the southern part of the Peninsula (e.g., Londa, Bababudan, Shevaroy, Nilgiris and Palni hills; Figs. 1 and 2). Remnants of a second younger landsurface are found downslope Al-Fe duricrust relicts. They are capped by weathering profiles topped by a Fe duricrust or by a Fe-Mn duricrust if an underlying Mn-protore is present (Fig. 2). The third and last lateritic paleolandsurface on the highland is a pediment, which is capped by reworked debris of lateritic duricrusts (Fig. 2). The debris may be cemented to form a ferricrete, or a Fe-Mn duricrust, if Mn ore debris are also included in the pediment sedimentary cover above a Mn-protore (see below). Following weathering and abandonment of the pediment, the lateritic covers of the highland have been essentially stripped and incised by rivers, leaving only sparse relicts of the three paleolandsurfaces (Radhakrishna, 1993). The lowland pediment is underlain by a weathering profile that locally hosts bauxite and Mn ore pockets and is capped by a ferricrete, which may be a Fe-Mn duricrust above Mn-protores (Beauvais et al., 2016).

Four Mn-ore deposits were visited and sampled on the highland and three in the lowland (Fig. 1). Two actively operated Mn-ore deposits (Kappataswamy and Channanghi KMK-E) were sampled in the highland Sandur massif (Figs. 1 and 2b; stars 1 and 2; Table 1). Lateritic Mn-ore deposits developed upon Late Archean protores younger than 2651 ± 18 Ma, as constrained by SHRIMP U-Pb dating of their stratigraphically underlying volcanics (Nutman et al., 1996). The protores include phyllites, argillites, arenites and Fe-Mn stromatolitic carbonates that yielded a 2475 ± 65 Ma Pb-Pb isochron age (Chadwick et al., 1996; Russell et al., 1996). The open pits are weathering profiles excavated into a remnant of the second paleolandsurface capped by a Fe-Mn duricrust, at 1012-1015 m elevation (Figs. 2b; 3a and 3b). A remnant of the first paleolandsurface dominates the deposit at ca. 1100 m elevation (Fig. 2b).

Highland samples were also collected closer to the WGE, in two abandoned mines of the Shimoga area (Triveni and Kumsi Mn ore open pits; Figs. 1 and 2a, stars 3 and 4, respectively, see also 3c-d and Table. 1). In these pits, the protore is a metavolcanic rock belonging to the Shimoga greenstone belt (Rb-Sr isochron age of 2520 ± 62 Ma; Bhaskar Rao et al., 1992). The protore also comprises Mn-phyllites, which weathered during the Cenozoic as constrained by palynological analyses (Krishna Rao et al., 1982). The Triveni Mn ore samples (Fig. 2a) have been collected at altitudes between 850 and 875 m (Table 1) in the Fe-Mn duricrust-capped weathering profile of the second paleolandsurface (Fig. 2a). The Kumsi pit exposes a 21 m thick lateritic profile of a relict of the pediment forming the third highland paleolandsurface (~ 710 m altitude; Figs. 2a and 3d). The sampled profile consists in a ~ 6 m thick dismantled lateritic duricrust hosting a ~ 2 m thick sedimentary layer mixing decimetric ferruginous, manganiferous clasts and infracentimetric oolites (Fig. 3d) upon ~ 15 m of massive Mn-ore.

The weathering profile of the lowland pediment developed upon greenstones similar to those of the Shimoga belt (Dessai, 1985; Fig. 1) and were constrained by paleomagnetism as “late Paleogene to Neogene” in age by Schmidt et al. (1983). The elevation of the pediment varies from 200 m at the foot of the WGE to 50 m close to the coastline (Fig. 2c). We collected samples in four pits excavated in the pediment capping ferricrete (Caurem, star 5, Naveli 1 and Naveli 2, star 6, and Cudnem, star 7; Figs. 1 and 2c; see also Table. 1). Caurem, Naveli 1&2 and Cudnem pits have been excavated where the ferricrete lies at 100 m, 140 m and 50 m elevation, respectively. In those pits, the weathering profile is 25 to 100 m thick and the ferricrete is made of cemented reworked lateritic clasts (Figs. 3e-f-g; Babu, 1981; Bonnet, 2015).

2.2. Samples preparation, characterization and analysis

Potassium-rich end-member of coronadite group (i.e., cryptomelane) from the hollandite supergroup (Biagioni et al., 2013), is a common supergene Mn-oxide of the lateritic Mn-ore deposits of southern India (e.g., Krishna Rao et al., 1982; Mohapatra et al., 1996) which can be used for $^{40}Ar/^{39}Ar$ dating. The crystallographic system of this mineral allows argon gas retentiveness in a tunnel-type crystal lattice, which is characterized by a double chain of MnO_6 octahedra and K^+ cations in the large tunnel lacuna to insure the electronic neutrality of the lattice (Turner and Buseck, 1979; Post and Burnham, 1986). Tunnel oxides retained efficiently Ar and K and remain close in supergene environmental conditions (Vasconcelos, 1999b; Vasconcelos et al., 1994), leading to meaningful crystallization age of the minerals. However K-rich Mn-oxides are usually mixed with other oxides, such as others Mn-oxides (e.g., pyrolusite, lithiophorite) and Fe-oxides (hematite, goethite). Therefore, careful observations and extraction techniques are required to ensure meaningful dating.

The method implemented to characterize and separate the K-rich Mn-oxides grains from field samples is summarized in figure 4. Field samples were cut with a circular saw (1.5 mm breadth) to get a section allowing accurate observations. A 200-300 µm thick polished thin section and a symmetrical 500 µm thick slab were made from each sawed fragment. Polished thin sections have been studied using reflected light microscopy (Fig. 5a-g). We also used elemental cartography by X-ray micro-fluorescence (µ-XRF) with a XGT7000 Horiba Jobin Yvon producing a high-intensity beam with a 100 µm spot size, Rh X-ray tube, accelerating voltage of 30 kV and current of 1mA. Micro-XRF elemental maps of Fe, K and Mn are stacked together on a single image using ImageJ software by assigning a distinct color to each elemental map (Figs. 4 and 6). The resulting images are helpful to locate K-rich phases on the slab. Electron Probe Micro-chemical Analysis (EPMA) of minerals using a CAMECA SX-100 electron microprobe equipped with five wavelength-dispersive X-ray spectrometers (WDS) provided the precise micro chemical composition of K-Mn oxides.

Grains were then separated from the slabs using a micro-drill under a large magnifier (Fig. 4). Some of them were observed with a scanning electron microscope (SEM, Fig. 5h), other were crushed to produce a powder sieved at 64 µm, which was analyzed by XRD using a Panalytical X'Pert Pro MPD with a Co Kα X-ray source (λ = 1.79 Å) operating at 40kV and 40 mA. The remaining grains were ultrasonically cleaned in absolute ethanol, conditioned in aluminum foil packets and placed into a irradiation vessel along with $^{40}Ar/^{39}Ar$ dating standard Taylor Creek Rhyolite sanidine 2 (TCRs-2) monitor, dated at 28.608 ± 0.033 Ma (Renne et al., 2011). Irradiation took place in the TRIGA Mark-II reactor of Pavia University (Italy) during 50 hours. Prior experiments have shown none or very little ^{39}Ar recoil from those grains.

Isotopic analyses were then performed on irradiated K-rich Mn-oxide separates using either step heating degassing under a CO_2 laser probe coupled with an Argus VI multicollection mass spectrometer (with 4 faradays for masses ^{40}Ar-^{37}Ar and ion counting on ^{36}Ar) or a step-wise heating procedure in a double vacuum Staudacher-type furnace coupled with a VG3600 mass spectrometer using peak jumping and Faraday/Daly analyzer as described by Arnaud et al. (2003). Mass discrimination of machines and blank levels are followed daily. Isotopic ratios were corrected for irradiation interferences and air contamination using a mean air value of 298.56 ± 0.31 (Lee et al., 2006; Renne et al., 2009).

Ages were statistically analyzed in three ways: ^{39}Ar release spectra, inverse isochrons (Table. 2) and age's frequency or probability plots. Age spectra detail the homogeneity of argon released and age stability throughout the degassing process, with the prior assumption of atmospheric correction for inherited argon. When apparent ages are integrated over continuous steps overlapping at the 2σ level and releasing at least 70% $^{39}Ar_K$, the derived plateau age is statistically robust and meaningful (e.g., Beauvais et al., 2008). However, when plateau is derived from less than 70% of $^{39}Ar_K$ released (e.g., Vasconcelos, 1999a; Li and Vasconcelos, 2002; Vasconcelos and Conroy, 2003; Colin et al., 2005), the critical value of 50% $^{39}Ar_K$ released is accepted to calculate a "plateau age" (e.g., Li et al., 2007; Feng and Vasconcelos, 2007; Vasconcelos et al., 2013; Riffel et al., 2014; Bonnet et al., 2014; Deng et al., 2016) provided that it is integrated over three or more continuous steps whose ages overlap at the 2σ level (Fleck et al., 1977; Maluski, 1985; McDougall and Harrison, 1999). When more than two apparent steps overlaps at the 2 σ level but integrate only 40 to 50% of the $^{39}Ar_K$ released, "pseudo plateau" are defined and considered as acceptable and meaningful (Vasconcelos et al., 2013; Riffel et al., 2014).

When those criteria are not satisfied but barely missed (ages do not strictly overlap at the 2 σ level) a "forced plateau" integrating more than two consecutive reasonably flat steps is calculated with a weighed mean (weighed by the error and the

^{39}Ar released in each step) (see Feng and Vasconcelos, 2007; Vasconcelos et al., 2013; Riffel et al., 2014). The $^{36}Ar/^{40}Ar$ vs. $^{39}Ar/^{40}Ar$ correlation diagrams (also called inverse isochrons) are also used to derive the best-fitted inverse isochron (Roddick et al., 1980) allowing to estimate a statistically robust age. The inverse isochron approach also is particularly useful to detect different contamination from various excess or inherited argon reservoirs, which may result from atmospheric argon incorporated in the less retentive site of the grain, or excess ^{40}Ar released from older K-bearing minerals. For some authors (De Putter et al., 2015), best inverse isochrons exclude the first heating steps, which are usually dominated by trapped atmospheric Ar in the less retentive crystalline sites. These ages are derived from best-fitted inverse isochrons that should have mean square weighted deviation (MSWD) as close as possible to 1 with regard to the distribution of points and their absolute error, but this value is not a limitation to derive an acceptable inverse isochron. Regressions are classically accepted as significant when MSWD is less than 2.5 (Roddick et al., 1980), possibly around 1. There is therefore a complicated trade-off between the number of points used, the MSWD, and the use of the most radiogenic $^{40}Ar^{*}$ rich steps.

3. Results and interpretations

3.1. Petrological and geochemical characterization

Descriptions of samples and K-Mn oxide grains are compiled in the table 1. Two main petrographic forms of manganese ore can be distinguished. Float (very porous) or platty Mn-ores show the original banding of the siliceous phyllitic protore (Figs. 3a and 5a; Mishra, 1978; see also Bonnet et al., 2014). Mn-ore can also be massive podiform and botryoidal filling micro porosities (Fig. 5b and Fig. 6a-b) and larger cavities, in which geodes formed by successive overgrowth of colloidal microstructures (Fig. 5e-f and Fig. 6a) becoming massive cryptocrystalline when cavities are totally filled (Fig. 5b-c). Colloidal overgrowth around nucleus (e.g. iron oxide, clasts) can also form massive nodules where the initial protore structure is totally erased (Fig. 5d-e).

Cryptomelane EPMA data are plotted in a ternary diagram (Fig. 7; see also the data repository DR1). Cryptomelane from Shimoga and Goa is enriched in aluminum (Fig. 7). The differences in alumina result either from contrasted parent rocks composition (e.g., carbonates without alumina vs. aluminous metavolcanic phyllites) or possible intergrowth with lithiophorite (Fig. 5e-g and Fig. 6a) or even gibbsite (Fig. 5h). These differences may also indicate a better maturation of Sandur's cryptomelane rich ores (Fig. 6), which are devoid of aluminous impurities (e.g., Beauvais et al., 1987).

3.2. Deciphering the $^{40}Ar/^{39}Ar$ age spectra

The different types of ^{39}Ar release spectra are shown in figures 8 and 9. Many samples yielded a regular flat age spectrum (Fig. 8a). As explained above, plateau ages are validated when at least three consecutive steps comprising up to 50% of total $^{39}Ar_K$ released overlap at the 2σ confidence level.

Degasing spectra may show evidence of negligible amount of ^{39}Ar, low % $^{40}Ar^*$ and large amount of atmospheric ^{40}Ar in the low energy degassing steps that generally increases the 2σ error of the first apparent ages (Fig. 8a). Another issue is the rejuvenated ages frequently observed at low temperature steps (Fig. 8b), which can be the result of a loss of $^{40}Ar^*$ from less retentive and poorly crystallized sites (see (Vasconcelos, 1999b). But most of the time the apparent ages progressively reach a constant value at higher temperature steps allowing definition of a plateau, which is also well supported by an inverse isochron (see Fig. 8b). Sixteen samples show such a degasing spectrum integrating up to 90% of the total extracted signal, and excluding only the very first steps with ages lower than the plateau. These well-defined plateaus are used to calculate the absolute ages of the K-Mn oxides. Generally, both the ages estimated from spectra and inverse isochrons are equivalent (Fig. 8a-b, Table. 2). Therefore, we choose to present our ages only with ^{39}Ar release spectra that clearly show a plateau, and with both spectra and inverse isochrons when no clear plateau is identified. Plateau ages (70% $^{39}Ar_K$ released) and best-fitted inverse isochrons are considered as first order ages and noted (A) in figures 10, 11 and 12.

Some age spectra do not allow calculating a standard age plateau according to the definition of Fleck et al. (1977), but only a "forced-plateau" defined from ^{39}Ar release spectra encompassing four steps releasing ~ 70% (Fig. 8c). In other release spectra, a probable authigenic component ages the last steps, which result in an older intermediate step with several little pseudo plateaus (10 to 30 % ^{39}Ar each) of similar ages (Fig. 8d). In such cases, an estimated concordant pseudo-plateau age is often supported by a valid inverse isochron age (Table. 2; see also Bonnet et al., 2014). This can be a valid alternative when the total amount of integrated %$^{39}Ar_k$ is higher than 40% of the total signal. But such a concordant pseudo-plateau age should also be certified by a well-defined plateau age in another sample from the same weathering profile. Plateau ages integrating less than 70% $^{39}Ar_K$ released, "Forced plateau", "Pseudo plateau" and "concordant pseudo plateau" ages are considered as second-order ages noted (B) in figures 10, 11 and 12. Nevertheless, these ages are often validated by best-fitted inverse isochrons (Table 2) and are meaningful of first order weathering events.

When the age spectra present an obviously convex hump shape (Fig. 9a) the youngest and oldest apparent ages may result from a mixing between gases released from two phases (e.g., Ruffet et al., 1996; Hautmann and Lippolt, 2000; Vasconcelos and Conroy, 2003; Beauvais et al., 2008; De Putter et al., 2015). Possible argon loss from less retentive intercrystalline site could also affect these degasing patterns (Fig. 9a). The statistical analysis of both the age spectrum and the inverse isochron may help to estimate minimum and maximum ages of mixed phases (e.g., Bonnet et al., 2014). In the case of sample TRI-3a the only possible inverse isochron yields a maximum estimate of the youngest phase at ~ 11 Ma (Fig. 9a). However, this age is not validated by a well-defined plateau age from another sample of the same deposit (Fig. 11), and therefore noted (C). Most spectra with a hump-shape also show a plateau integrating at least 50% of $^{39}Ar_K$ in the intermediate energy levels but the derived age is a minimum estimate of the oldest phase (e.g., KUM-4oo, Fig. 11; see also NAV-3c and NAV-3b Fig. 12). The plateaus included in these hump-shape spectra should be considered more carefully and derived ages are noted (B), but acceptable inverse isochrons are derived (Fig. 12, Table 2). Other hump shape spectra exhibit young apparent ages forming “pseudo plateaus” in low and high energy levels with concordant ages, which bracket an older plateau age in the intermediate energy level (e.g., CAU-1a, CAU-1c, CAU-3a, CAU-2, Fig. 12, Fig. 12). The correlation diagrams for these samples point to possible inverse isochrons estimating maximum and minimum age of the youngest and oldest mixed-phases respectively (Fig. 12, Table 2). For example, the oldest phases with minimum ages ~ 22 to ~ 24 Ma (Fig. 12) are probably contaminated by youngest phases with maximum age ~ 19 to 20 Ma. These ages are noted as (B) and meaningful when derived from best-fitted inverse isochrons and/or plateau integrating at least 50% $^{39}Ar_K$.

On another hand, the age difference between the youngest and oldest phases is larger (e.g., KPA-2.5, Fig. 10; see also CAU-1b, Fig. 12), ages estimations are too speculative and only the minimum age of the oldest phase can be estimated and noted with a (C) in figures 10, 11 and 12 (see also Table 2). These ages are not meaningful.

Other samples show "saddle shape" spectra (Figs. 9b-c) with a progressive decrease of the apparent ages in the intermediate energy steps and a very large increase of the ages at highest energy steps. This complex type of spectra may result from significant ^{39}Ar loss by recoil and/or contamination (Turner and Cadogan, 1974; Vasconcelos, 1999b; Vasconcelos and Conroy, 2003). The high energy steps suggest a hypogene contaminant (Vasconcelos et al., 1994; Ruffet et al., 1996; Li and Vasconcelos, 2002; Bonnet et al., 2014), which can also age the other steps (e.g., Fig. 9c). Most of these spectra display overestimated ages, which are not reliable (Vasconcelos and Conroy, 2003). Noted that no inverse isochron is derivable, the correlation diagram showing at best a mixing of inherited contaminant and supergene phase (Fig. 9c).

The Table 2 synthetize the results and shows 24 well defined plateaus ages (> 70% $^{39}Ar_K$) with one best-fitted inverse isochron age noted (A). In addition 18 ages noted (B) are also derived either from "plateaus" and "forced plateaus" (at least 50% $^{39}Ar_K$) or from "concordant pseudo plateaus" ages and best-fitted inverse isochrons. All these ages are reliable and geologically significant and have been plotted against altitude, and combined with individual age probability diagram (Fig. 13a) that enhances most probable weathering age peaks (Vasconcelos, 1999b).

3.3. $^{40}Ar/^{39}Ar$ geochronology of lateritic weathering in South India

Here we present 29 newly analyzed K-Mn oxide grains that are interpreted together with grains studied by Bonnet et al. (2014) and Beauvais et al. (2016) (Table 2 and Fig. 13a). The total analysis of 46 Mn-oxide grains provides 40 age spectra with significant geological meaning as “plateaus”, “forced-plateaus”, “pseudo plateau” “concordant pseudo-plateaus” or “hump shape”. We present our results in three figures grouping age spectra obtained from K-Mn oxide grains of the Sandur (Fig. 10), Shimoga (Fig. 11) and Goa deposits (Fig. 12). All the ages are also presented in Table 2 including the best inverse isochron age estimates (See also data repository tables DR2 and DR3).

3.3.1. $^{40}Ar/^{39}Ar$ ages from highland Sandur Mn ore deposit

Among all the samples dated in the Sandur Mn ore deposit, 18 samples show plateau ages noted (A). The ages range from ~ 26 Ma (KMK-3) to ~ 53 Ma (KPA-8) (Fig. 10 and Table 2). Two age groups are distinguished: ~ 53 - 50 Ma and ~ 37 - 26 Ma (Fig. 10). Two spectra have a “hump shape” resulting from mixed supergene phases (Bonnet et al., 2014; Hautmann and Lippolt, 2000; Ruffet et al., 1996; Vasconcelos et al., 1995). The spectrum of sample KPA-2.5 shows a maximum apparent age ~ 46 Ma old, which is a minimum estimate of the oldest phase in the mixing. In sample KPA-12a minimum age of ~ 34 Ma noted (C) for the oldest phase is coherent with plateau ages (A) between ~ 37 Ma (KMK-3b) and ~ 32 Ma (KPA-11) (Fig. 10), which are attributed to the second weathering period. Nine grains display plateau-ages between ~ 26 and ~ 30 Ma. The high frequency of these ages is linked to the analysis of several aliquots of samples KPA-10 (4 grains) and KPA-12a (6 grains), which yielded reproducible plateaus, and also allowed quantifying the growth rate for these cryptocrystalline colloidal structures. Grains KPA-12a1 and KPA-12a5 are separated by 12.2 ± 0.1 mm (Figs. 6 and 10) and the estimated growth rate of the massive cryptocrystalline colloidal structure is 5.7 ± 3 mm. Ma^{-1}. A mean rate of 5.0 ± 4 mm. Ma^{-1} in botryoidal overgrowth microstructure was also estimated for sample KPA-10 between grains KPA-10a and KPA-10c (Figs. 6 and 10). These rates are comparable with earlier growth rate estimates of 6.4 ± 1.2 mm. Ma^{-1} (Vasconcelos et al., 1992) or 1 to 5 mm. Ma^{-1} (Hénocque et al., 1998).

3.3.2. $^{40}Ar/^{39}Ar$ ages from highland Shimoga Mn ore deposits

The obtained ages are mostly comprised between ~ 30 and 24 Ma (Fig. 11). However, one grain (KUM-4oo) displays a spectrum with a singular hump shape, which results from a mixing of two phases (Figs. 11a-b). The "forced plateau" age at ~ 39 Ma including 58% of the total amount of ^{39}Ar released is the minimum estimate of the oldest phase and noted (B), which is also supported by the sole possible inverse isochron with a MSWD value less than 2.5 (Fig. 11b). The correlation diagram does not allow estimating an acceptable age for the youngest phase in this mixed grain (Table 2). The considered grain was picked up from a lateritic clast reworked in the lateritic pediment topping the Kumsi Mn-ore deposit (site 4 on Fig. 2a). The detrital nature of this sample and its high porosity are attested by reflected light microscopy (Fig. 5d). This suggests provenance from a lateritic Mn-duricrust previously exposed on a higher landsurface, which was dissected and eroded allowing lateritic clasts transport and deposition at lower elevations on the pediment in which the Kumsi pit is excavated. Therefore, the Kumsi pediment must be younger than 39 Ma (minimum age of the oldest phase in KUM-4oo) but older than 26 Ma (most common age of the youngest phase in the same profile, Fig. 11a and Table 2). Sample TRI-3b (Fig. 11) shows a middle spectrum portion with ages ranging from ~ 43 to ~ 48 Ma accounting for 70% of the total ^{39}Ar released. An inherited phase seems to release gas especially at high energy step heating, but when this phase started to degas at lower energy, the apparent ages at intermediate heating steps are artificially aged that increases the apparent age up to ~ 48 Ma. The best age estimation of the supergene phase in this grain is most probably ~ 43 Ma but must be considered only as a maximum age estimate.

The release spectrum of samples KUM-3f and KUM-2 show weakly aged steps at the beginning of the analysis, which possibly resulted from minor ^{39}Ar recoil (Turner and Cadogan, 1974). However, the disturbance is very low and meaningful age at ~ 30 Ma (KUM-3f) and ~ 23 Ma (KUM-2) both by a pseudo plateau (Fig. 11a) and well-constrained inverse isochrons (Fig. 11b; Table. 2). Several aliquots of samples TRI-3 and KUM-3a (Fig. 11) yield consistent plateau ages of 25.5 Ma and ~ 26-27.5 Ma, respectively.

3.3.3. ^{40}Ar/^{39}Ar ages from lowland Goa Mn ore deposits

The cryptomelane ages from samples of the lowland Mn-ore deposits are distributed in two main age groups. The first group comprises two-ages at ~ 47 and 45 Ma, obtained for two aliquots of sample NAV-3, which are probably minimum estimates. The spectrum of NAV-3c allows integrating 60% of the total amount of ^{39}Ar released overlapping at the 2σ error (Fleck et al., 1977) that yields a plateau age (A) of 47.0 ± 0.6 Ma, which is supported by the inverse isochron age (Table 2 and Fig. 12b). Further evidence of early weathering around ~ 45 Ma (minimum age of NAV-3b) in the lowland is supported by the spectrum and a possible inverse isochron (Fig. 12). The spectrum of sample CAU-1b (Fig. 12) also shows a maximal apparent age at ~ 45 Ma, which is a minimum age and should be noted (C). The old ages are systematically obtained from samples collected in the deepest part of the weathering profile. Younger ages between ~ 19 Ma and ~ 24 Ma (group 2) and discrete ages at ~ 8.7 Ma and 2.5 Ma are also identified (Fig. 12). All these ages are supported by inverse isochron ages (see Table. 2).

Sample CAU-2 shows a “hump shape” explained by the probable mixing of two phases, with a minimum age of ~ 24.5 Ma for the oldest and a maximum estimate of ~ 19 Ma for the youngest. The oldest estimate cannot be validated by inverse isochrons (Fig. 12b, and Table 2). In three similar cases, secondary pseudo-plateaus at ~ 20 Ma can be detected on either side of a plateau or a “forced plateau” (e.g., CAU-2). For example, sample CAU-3a (Fig. 12) shows a plateau at ~ 24 Ma, which is a minimum estimate flanked by small concordant pseudo-plateaus at ~ 19-20 Ma in low- and high-energy steps accounting together for 32% ^{39}Ar degassed. Sample aliquots CAU-1a and CAU-1c (Fig. 12) also show similar “hump shape” type spectra with a plateau age flanked by concordant pseudo-plateau ages suggesting mixing of two phases of different ages (Vasconcelos et al., 1995; Ruffet et al., 1996; Hautmann and Lippolt, 2000) but close enough to be grouped in the same weathering period ca. 19 to ca. 24 Ma. However, for these last three samples the difference between the oldest and the youngest phase (20 Ma) is small enough to allow deriving three minimum plateaus ages noted (B) at ~ 24 Ma associated with three concordant (B) maximum ages at ~ 20 Ma (Fig. 12). The youngest ages ~ 20 Ma are rather well supported by reliable inverse isochron ages (Table. 2, Fig. 12b).

3.3.4. Interpretation of the $^{40}Ar/^{39}Ar$ ages

The first- and second order (A and B) $^{40}Ar/^{39}Ar$ ages allow defining three main lateritic weathering periods (W1, W2a and W2b) in South India (Fig. 13a). The first weathering period W1 (ca. 53 to ca. 45 Ma) corresponds to intense chemical rock weathering upon both the highland and the lowland. Intense (bauxitic) weathering of the first paleolandsurface is interpreted as correlative to this weathering period (Bonnet et al., 2014; Krishna Rao et al., 1989b). The second weathering period W2 from ca. 37 to ca. 19 Ma may be divided in two stages, W2a (ca. 37-26 Ma) mostly in the highland (Sandur, ca. 37-26 Ma and Shimoga, ca. 30-26 Ma) and W2b (ca. 26-19 Ma) only in the western highland (Shimoga, ca. 26-23 Ma) and in the lowland (Goa, ca. 24-19 Ma). The early stage (W2a) characterizes late Eocene to late Oligocene lateritic weathering of the second highland paleolandsurface, as best recorded in the eastern part (Sandur), and more discretely in Shimoga (e.g., ca. 30 Ma from KUM-3f, Fig. 11b). This weathering period also led to maturation of the previously formed bauxitic weathering profiles (e.g., Krishna Rao et al., 1989b). After 26 Ma, the Sandur remnants of the two oldest paleolandsurfaces do not seem to be longer subject to weathering, while the western highland landscape (Shimoga) still weathered until ca. 23 Ma at the time the lowland weathered too. Two later minor Late Neogene weathering pulses are also recorded in the lowland (9 and 2.5 Ma).

The weathering periods would sign installation of wet and warm climate leading to thick soil development under rainforest conditions over the peninsula, whereas the time intervals between these weathering periods may be interpreted as episodes of subdued chemical weathering and correlative higher mechanical erosion and landscape dissections (e.g., Beauvais and Chardon, 2013). Such climate driven erosion processes changes have resulted in the installation and preservation of the successive lateritic paleolandsurfaces over South India. The first, bauxitic paleolandsurface, was essentially shaped until a maximum age of ca. 45 Ma by intense weathering and only slightly reworked and dissected after that time during the shaping, and later weathering of the second landsurface between ca. 37 and ca. 26-23 Ma. Finally, abandonment / dissection of the highland pediment after ca. 23 Ma indicates that the thick lateritic covers of South India formed in the Eocene and Oligocene and that stripping of that material and intense dissection of the peninsula essentially took place in the Neogene (i.e., after 23 Ma).

4. Morphoclimatic implications of $^{40}Ar/^{39}Ar$ dating

Periods of intense weathering have affected the highland landscapes during the early Eocene, and from late Eocene to late Oligocene. By contrast, the lowland weathered mostly during the early Eocene and the early Miocene (Fig. 13a). The successive Eocene to early Miocene weathering periods documented by the present study coincided with the northward migration of India across the humid equatorial belt (Fig. 13b). Early Eocene bauxitic weathering also coincided with the Eocene climatic optimum (Fig. 13c), at a time of relatively high atmospheric CO_2 (Pearson and Palmer, 2000), North Atlantic rifting (62 to 55 Ma) and the subduction of Tethysian carbonates (Van der Voo et al., 1999).

4.1. Early Eocene lateritic weathering (ca. 53-45 Ma; W1)

The $^{40}Ar/^{39}Ar$ ages indicate that lateritic weathering started at least ~ 50 Ma ago over the highland and ~ 47 Ma in the lowland (Figs. 10, 12 and 13a). Preserved laterites as old as 47 Ma under the lowland pediment argue for Early Eocene installation and stabilization of the Western Ghats Escarpment with a lateritic pediment on its piedmont (Beauvais et al., 2016). The old ages (ca. 53 to ca. 45 Ma) also document synchronous lateritic weathering in the lowland and the highland (Beauvais et al., 2016), when India drifting slowed down at the onset of the collision with Asia ~ 50 Ma ago (e.g., Zhu et al., 2005; Rowley and Currie, 2006). In the meantime, India also entered a latitudinal range where water precipitation was higher than evaporation (Fig. 13b) propitious to the development of equatorial and/or tropical warm and humid forest (Kent and Muttoni, 2008; see also Patriat and Achache, 1984; Manabe and Bryan, 1985; Tardy and Roquin, 1998; Chatterjee et al., 2013) that further enhanced lateritic weathering. At the time of India-Asia collision, CO_2 degassing of pelagic carbonate into the atmosphere ceased with the end of the North Tethys subduction (Caldeira, 1992) concomitantly with intense continental (bauxitic) lateritic weathering worldwide (Prasad, 1983; Valeton, 1999; Retallack, 2010) and correlative offshore carbonate production (e.g., Chaubey et al., 2002 for the West Indian margin). Bauxitic weathering was effectively documented by $^{40}Ar/^{39}Ar$ cryptomelane ages throughout the tropical belt during the Eocene e.g., from 56 to 51 Ma in South America (Ruffet et al., 1996; Vasconcelos, 1999b; Vasconcelos et al., 1994) and from 59 to 45 Ma in West Africa (Hénocque et al., 1998; Colin et al., 2005; Beauvais et al., 2008). Combined together, all these concomitant phenomena consumed high quantities of atmospheric CO_2 (Dessert et al., 2003) that progressively cooled the climate once past the Eocene Climatic Optimum (Kent and Muttoni, 2008, 2012; see also Zachos et al., 2001, 2008). In turn, progressive climate cooling from Mid-Eocene onward (Fig. 13c) has favoured the dissection of early Eocene bauxitic landscapes.

4.2. Late Eocene-late Oligocene weathering (ca. 37-26 Ma; W2a)

This first weathering stage of period W2 is marked mostly in the highland, particularly by two prominent peaks at ~ 28 Ma and ~ 26 Ma in the Sandur massif and the Shimoga area, respectively (Fig. 13a), and more speculatively in the lowland if we consider that 24 Ma is a minimum age. This episode (37-26 Ma) is interpreted to reflect the continental weathering response to the late Oligocene warming (Fig. 13c) at a time of a marine transgression propitious to offshore carbonate production (Biswas, 1987). Thickening of the proto-Himalaya since ~ 40 Ma (Aikman et al., 2008) resulted in the installation of an orographic barrier (Molnar et al., 1993; Ramstein et al., 2005), which redistributed the humid air masses southward (Dupont-Nivet et al., 2008). A monsoonal regime installed at that time in Southern Asia (Licht et al., 2014) that could intensify weathering processes on the Indian peninsula. Under such climatic conditions, the lateritic weathering profiles underlying remnants of the first two paleolandsurfaces became less well drained as a result of river incision, but did not become totally inactive, as attested by younger dates in Sandur, e.g., ca. 37 to ca. 26 Ma (Figs. 10 and 13a). During this period, the early Eocene bauxites have still evolved on the highland (Krishna Rao et al., 1989b; see also Bonnet et al., 2014) at least until global cooling by ~ 34 Ma (Fig. 13c; Molnar and England, 1990; Zachos et al., 2001).

Early Oligocene cooling also coincided with a sea level fall (Chaubey et al., 2002), and the installation of dryer climatic conditions (see Fig. 13c), which may have resulted in the attenuation of the weathering intensity observed between 32 and 29 Ma in the highland (Fig. 13a). The highland pediment may possibly have been formed in this time interval, and subsequently weathered between 29 and 23 Ma. At that time, the lowland landscape was also possibly rejuvenated, but previously formed lateritic weathering mantles as old as ca. 47-45 Ma were preserved (Figs. 12 and 13a), attesting to a very slow denudation regime of the pediment below the WGE (Beauvais et al., 2016). The contrasted weathering record of the highland and the lowland after the Mid-Eocene (Fig. 13a) suggests a spatial contrast in rainfall distribution on either side of the WGE. This contrast was mostly controlled by dominant South-East moisture fluxes during the late Eocene and the early Oligocene (Licht et al., 2014; Chen and Li, 2014) before installation of modern monsoon regimes in the early Miocene (Clift et al., 2008), which reactivated weathering preferentially in the lowland.

4.3. Late Oligocene-Early Miocene weathering (ca. 26-19 Ma; W2b)

This second stage of weathering period W2 is mostly marked in the western highland and the lowland. Weathering in eastern highland lateritic profiles of the Sandur massif definitively ceased at ca. 26 Ma (Bonnet et al., 2014), while the western part of the highland adjacent to the WGE (Shimoga) possibly weathered until ca. 23 Ma (Fig. 13a). Therefore, the highland lateritic pediment carrying those profiles has been incised essentially after 23 Ma at a rate < 5 m/m.y. (Figs. 2a-b). During highland incision, lateritic weathering was reactivated on the lowland pediment with a peak activity at ~ 19-21 Ma (Fig. 13a). Central Asia aridification started ~ 24 Ma ago (Sun et al., 2010). Highland weathering mitigation after ~ 23 Ma may be due to such a change in climatic regime, which increased the east-west wetness gradient over peninsular India and signed the onset of modern-like monsoonal regimes (Clift et al., 2008; see also Chatterjee et al., 2013).

The lack of reliable ages between ~ 19 Ma and 9 Ma (Fig. 13a) suggests that weathering is not recorded or preserved in peninsular India during Mid-Miocene. After the early Miocene (i.e., after ca. 16 Ma), a significant change has been however observed in the clay content of sediments from the neighbouring Arabian Sea, wherein illite became dominant compared to kaolinite and smectite (Phillips et al., 2014). This, together with our results, indicates an attenuation of continental weathering and suggests dominant landscape dissection of the highland. By contrast, the lowland lateritic pediment was only slightly dissected after ~ 19 Ma (Beauvais et al., 2016). The weathering pulses at ~ 9 Ma and ~ 2.5 Ma (Figs. 12 and 13a) may be linked to Late Neogene intensification of the Asian monsoon in the sub region (Zhisheng et al., 2001), which may have been driven by uplift of the Tibetan plateau (Molnar et al., 1993; see also Clift et al., 2008).

5. Conclusion

The $^{40}Ar/^{39}Ar$ dating of supergene cryptomelane formed *in situ* in lateritic weathering profiles of Peninsular India sheds light on the Cenozoic weathering and erosion history of the subcontinent's surface. Cryptomelane ages document three major periods of weathering, i.e., early Eocene (W1) both on the highland and the lowland, ~ late Eocene – late Oligocene (W2a), only in the highland, and early Miocene (W2b), mostly in lowland. The $^{40}Ar/^{39}Ar$ age series suggest subdued relief production and dominant weathering of the highland before ~ 23 Ma and its dissection and stripping after that time, while the lowland weathered in the Early Eocene and Miocene before being slightly incised after ~ 19 Ma. The oldest ages (53-45 Ma) indicate widespread Eocene lateritic weathering in South India at the time of global Eocene climatic optimum, when the peninsula crossed the equatorial belt. Our results also document the installation of a dual climatic regime across the Western Ghats escarpment after the Eocene climatic optimum, leading to divergent weathering and erosion patterns on both sides of this topographic barrier. Hence, K-Mn oxides $^{40}Ar/^{39}Ar$ age series document the tempo of South Indian morphogenesis, and as such may be viewed as a proxy for erosion and climatically driven weathering over geological time scales.

Acknowledgements- This work was funded by Indo-French Centre for the Promotion of Advanced Research (IFCPAR) project 5007-1, the IRD (UR 161) and the CNRS (INSU 2011-CT2). The French Ministry for the Scientific Research and Education granted N.J. Bonnet a Ph.D. scholarship (ED251, Aix Marseille Université, Observatoire des Sciences de l'Univers Pytheas). N.J. Bonnet was also supported by a fellowship from IFCPAR. We thank L. Giosan and an anonymous referee for their comments and suggestions, and editorial handling from F. Chabaux and Michael E. Böttcher.

References

Aikman, A.B., Harrison, T.M., Lin, D., 2008. Evidence for Early (> 44 Ma) Himalayan Crustal Thickening, Tethyan Himalaya, southeastern Tibet. Earth Planet. Sci. Lett. 274, 14–23. doi:10.1016/j.epsl.2008.06.038

Arnaud, N., Tapponier, P., Roger, F., Brunel, M., Scharer, U., Wen, C., Xu, Z., 2003. Evidence for Mesozoic shear along the western Kunlun and Altyn-Tagh fault, northern Tibet (China). J. Geophys. Res. 108, 2053. doi:10.1029/2001JB000904

Babu, P.V.L.P., 1981. Laterite as an unconformity plane in the evolution of the South Indian peninsula – a synthesis. In: International Seminar on Lateritisation Processes (Trivandrum, India 11-14 December, 1979). Balkema, Rotterdam, Netherlands pp. 302–307.

Bárdossy, G., Aleva, G.J.J., 1990. Lateritic bauxites. In: Developments in Economic Geology (27). Elsevier, Amsterdam, Netherlands, pp. 624.

Beauvais, A., Bonnet, N.J., Chardon, D., Arnaud, N.O., Jayananda, M., 2016. Very long-term stability of passive margin escarpment constrained by $^{40}Ar/^{39}Ar$ dating of K-Mn oxides. Geology 44, 299-302. doi:10.1130/G37303.1

Beauvais, A., Chardon, D., 2013. Modes, tempo, and spatial variability of Cenozoic cratonic denudation: The West African example. Geochem. Geophys. Geosystems 14, 1590–1608.

Beauvais, A., Melfi, A., Nahon, D., Trescases, J.J., 1987. Pétrologie du gisement latéritique manganésifère d'Azul (Brésil). Min. Deposita 22, 124–134. doi:10.1007/BF00204689

Beauvais, A., Ruffet, G., Hénocque, O., Colin, F., 2008. Chemical and physical erosion rhythms of the West African Cenozoic morphogenesis: The ^{39}Ar-^{40}Ar dating of supergene K-Mn oxides. J. Geophys. Res. Earth Surf. 113, F04007. doi:10.1029/2008jf000996

Bhaskar Rao, Y., Sivaraman, T., Pantulu, G., Gopalan, K., Naqvi, S., 1992. Rb-Sr ages of late Archean metavolcanics and granites, Dharwar craton, South India and evidence for Early Proterozoic thermotectonic event (s). Precambrian Res. 59, 145–170. doi:10.1016/0301-9268(92)90055-S

Biagioni, C., Capalbo, C., Pasero, M., 2013. Nomenclature tunings in the hollandite supergroup. Eur. J. Mineral. 25, 85–90. doi:10.1127/0935-1221/2013/0025-2255

Biswas, S.K., 1987. Regional tectonic framework, structure and evolution of the western marginal basins of India. Tectonophysics 135, 307–327. doi:10.1016/0040-1951(87)90115-6

Bonnet, N.J., 2015. Dynamique long-terme d'une marge continentale divergente (Les Ghâts Occidentaux de l'Inde péninsulaire) : Contraintes géochronologiques ^{40}Ar-^{39}Ar des paléosurfaces latéritiques. PhD thesis, Aix Marseille Université, France, pp. 286

Bonnet, N.J., Beauvais, A., Arnaud, N., Chardon, D., Jayananda, M., 2014. First ^{40}Ar/^{39}Ar dating of intense Late Palaeogene lateritic weathering in Peninsular India. Earth Planet. Sci. Lett. 386, 126–137. doi:10.1016/j.epsl.2013.11.002

Caldeira, K., 1992. Enhanced Cenozoic chemical weathering and the subduction of pelagic carbonate. Nature 357, 578–581. doi:10.1038/357578a0

Chadwick, B., Vasudev, V., Ahmed, N., 1996. The Sandur schist belt and its adjacent plutonic rocks implications for Late Archaean crustal evolution in Karnataka. J. Geol. Soc. India 47, 635–639.

Chardon, D., Jayananda, M., Chetty, T.R., Peucat, J.-J., 2008. Precambrian continental strain and shear zone patterns: South Indian case. J. Geophys. Res. 113, B08402. doi:10.1029/2007JB005299

Chatterjee, S., Goswami, A., Scotese, C.R., 2013. The longest voyage: Tectonic, magmatic, and paleoclimatic evolution of the Indian plate during its northward flight from Gondwana to Asia. Gondwana Res. 23, 238–267. doi:10.1016/j.gr.2012.07.001

Chaubey, A.K., Gopala Rao, D., Srinivas, K., Ramprasad, T., Ramana, M.., Subrahmanyam, V., 2002. Analyses of multichannel seismic reflection, gravity and magnetic data along a regional profile across the central-western continental margin of India. Mar. Geol. 182, 303–323. doi:10.1016/S0025-3227(01)00241-9

Chen, L., Li, J., 2014. ^{40}Ar/^{39}Ar ages and stable isotopes of supergene jarosite from the Baiyin VHMS ore field, NE Tibetan Plateau with paleoclimatic implications. Chin. Sci. Bull. 59, 2999–3009. doi:10.1007/s11434-014-0276-8

Clift, P.D., Hodges, K.V., Heslop, D., Hannigan, R., Van Long, H., Calves, G., 2008. Correlation of Himalayan exhumation rates and Asian monsoon intensity. Nat. Geosci. 1, 875–880. doi:10.1038/ngeo351

Colin, F., Beauvais, A., Ruffet, G., Hénocque, O., 2005. First ^{40}Ar/^{39}Ar geochronology of lateritic manganiferous pisolites: Implications for the Palaeogene history of a West African landscape. Earth Planet. Sci. Lett. 238, 172–188. doi:10.1016/j.epsl.2005.06.052

Deng, X.-D., Li, J.-W., Vasconcelos, P.M., 2016. ^{40}Ar/^{39}Ar dating of supergene Mn-oxides from the Zunyi Mn deposit, Guizhou Plateau, SW China: implications for chemical weathering and paleoclimatic evolution since the late Miocene. Chem. Geol. *in press* doi:10.1016/j.chemgeo.2016.02.009

De Putter, T., Ruffet, G., Yans, J., Mees, F., 2015. The age of supergene manganese deposits in Katanga and its implications for the Neogene evolution of the African Great Lakes Region. Ore Geol. Rev. 71, 350–362. doi:10.1016/j.oregeorev.2015.06.015

Dessai, A., 1985. An appraisal of the manganese ore deposits of Goa, India. Proc. Indian Natl. Sci. Acad. Part Phys. Sci. 51, 1021–1032.

Dessert, C., Dupré, B., Gaillardet, J., François, L.M., Allègre, C.J., 2003. Basalt weathering laws and the impact of basalt weathering on the global carbon cycle. Chem. Geol. 202, 257–273. doi:10.1016/j.chemgeo.2002.10.001

Dupont-Nivet, G., Hoorn, C., Konert, M., 2008. Tibetan uplift prior to the Eocene-Oligocene climate transition: Evidence from pollen analysis of the Xining Basin. Geology 36, 987. doi:10.1130/G25063A.1

Feng, Y.-X., Vasconcelos, P.M., 2007. Chronology of Pleistocene weathering processes, southeast Queensland, Australia. Earth Planet. Sci. Lett. 263, 275–287. doi:10.1016/j.epsl.2007.08.036

Fleck, R.J., Sutter, J.F., Elliot, D.H., 1977. Interpretation of discordant $^{40}Ar/^{39}Ar$ age-spectra of mesozoic tholeiites from antarctica. Geochim. Cosmochim. Acta 41, 15–32. doi:10.1016/0016-7037(77)90184-3

Grandin, G., 1976. Aplanissements cuirassés et enrichissement des gisements de manganèse dans quelques régions d'Afrique de l'Ouest. Mém. ORSTOM (82), Université de Strasbourg, Paris, France, pp. 276

Gunnell, Y., 1998. The interaction between geological structure and global tectonics in multistoreyed landscape development: a denudation chronology of the South Indian shield. Basin Res. 10, 281–310. doi:10.1046/j.1365-2117.1998.00072.x

Hautmann, S., Lippolt, H.J., 2000. $^{40}Ar/^{39}Ar$ dating of central European K–Mn oxides — a chronological framework of supergene alteration processes during the Neogene. Chem. Geol. 170, 37–80. doi:10.1016/S0009-2541(99)00241-7

Hénocque, O., Ruffet, G., Colin, F., Féraud, G., 1998. $^{40}Ar/^{39}Ar$ dating of West African lateritic cryptomelanes. Geochim. Cosmochim. Acta 62, 2739–2756. doi:10.1016/S0016-7037(98)00185-9

Kent, D.V., Muttoni, G., 2012. Modulation of Late Cretaceous and Cenozoic climate by variable drawdown of atmospheric *p*CO2 from weathering of basaltic provinces on continents drifting through the equatorial humid belt. Clim. Past Discuss. 8, 4513–4564. doi:10.5194/cpd-8-4513-2012

Kent, D.V., Muttoni, G., 2008. Equatorial convergence of India and early Cenozoic climate trends. Proc. Natl. Acad. Sci. 105, 16065–16070. doi:10.1073/pnas.0805382105

Krishna Rao, B., Muzamil Ahmed, M., Janardhana, M.R., 1989a. Age of manganiferous laterite of Uttara Kanada district, Karnataka. J. Geol. Soc. India 34, 413–420.

Krishna Rao, B., Satish, P.N., Sethumadhav, M.S., 1989b. Syngenetic and Epigenetic features and genesis of the beauxite-bearing laterite of Boknur-Navge, Belgaum district, Karnataka. J. Geol. Soc. India 34, 46–60.

Krishna Rao, B., Srinivasan, R., Ramachandra, B.L., Sreenivas, B.L., 1982. Mode of occurrence and origin of manganese ores of Shimoga district, Karnataka. J. Geol. Soc. India 23, 226–235.

Lee, J.-Y., Marti, K., Severinghaus, J.P., Kawamura, K., Yoo, H.-S., Lee, J.B., Kim, J.S., 2006. A redetermination of the isotopic abundances of atmospheric Ar. Geochim. Cosmochim. Acta 70, 4507–4512.

Licht, A., van Cappelle, M., Abels, H.A., Ladant, J.-B., Trabucho-Alexandre, J., France-Lanord, C., Donnadieu, Y., Vandenberghe, J., Rigaudier, T., Lécuyer, C., Terry, D., Adriaens, R., Boura, A., Guo, Z., Soe, A.N., Quade, J., Dupont-Nivet, G., Jaeger, J.-J., 2014. Asian monsoons in a late Eocene greenhouse world. Nature 513, 501. doi:10.1038/nature13704

Li, J.-W., Vasconcelos, P., 2002. Cenozoic continental weathering and its implications for the palaeoclimate: evidence from $^{40}Ar/^{39}Ar$ geochronology of supergene K–Mn oxides in Mt Tabor, central Queensland, Australia. Earth Planet. Sci. Lett. 200, 223–239. doi:10.1016/S0012-821X(02)00594-0

Li, J.-W., Vasconcelos, P., Duzgoren-Aydin, N., Yan, D.-R., Zhang, W., Deng, X.-D., Zhao, X.-F., Zeng, Z.-P., Hu, M.-A., 2007. Neogene weathering and supergene manganese enrichment in subtropical South China: An $^{40}Ar/^{39}Ar$ approach and paleoclimatic significance. Earth Planet. Sci. Lett. 256, 389–402. doi:10.1016/j.epsl.2007.01.021

Maluski, H., 1985. Méthode Argon 39 - Argon 40 : Principe et applications aux minéraux des roches terrestres In: Méthodes de Datation Par Les Phénomènes Nucléaires Naturels - Applications. Masson, Paris, France, pp. 341–372.

Manabe, S., Bryan, K., 1985. CO_2-induced change in a coupled ocean-atmosphere model and its paleoclimatic implications. J. Geophys. Res. 90, 689 – 707.

McDougall, I., Harrison, T.M., 1999. Geochronology and thermochronology by the $^{40}Ar/^{39}Ar$ method, 2nd ed., Oxford University Press, New York, USA, pp. 271.

Mishra, R.N., 1978. Exploration planing for Sandur manganese ores. J. Geol. Soc. India 19, 446–453.

Mohapatra, B.K., Rao, D.S., Nayak, B.D., Sahoo, R.K., 1996. Mineralogical and chemical characteristics of ferromanganese ores from Sandur, Karnataka, India. J. Mineral. Petrol. Econ. Geol. 91, 46–61. doi:10.2465/ganko.91.48

Molnar, P., England, P., 1990. Late Cenozoic uplift of mountain ranges and global climate change: chicken or egg? Nature 346, 29–34. doi:10.1038/346029a0

Molnar, P., England, P., Martinod, J., 1993. Mantle dynamics, uplift of the Tibetan Plateau, and the Indian Monsoon. Rev. Geophys. 31, 357. doi:10.1029/93RG02030

Nahon, D., 1991. Introduction to the petrology of soils and chemical weathering. Wiley-Interscience, New-York, USA, pp. 313.

Nutman, A.P., Chadwick, B., Krishna Rao, B., Vasudev, V.N., 1996. SHRIMP U/Pb zircon ages of acid volcanic rocks in the Chitradurga and Sandur Groups, and granites adjacent to the Sandur Schist Belt, Karnataka. J. Geol. Soc. India 47, 153–164.

Ollier, C.D., 1988. Deep Weathering, Groundwater and Climate. Geogr. Ann. Ser. Phys. Geogr. 70, 285–290. doi:10.2307/521260

Patriat, P., Achache, J., 1984. India–Eurasia collision chronology has implications for crustal shortening and driving mechanism of plates. Nature 311, 615–621. doi:10.1038/311615a0

Pearson, P.N., Palmer, M.R., 2000. Atmospheric carbon dioxide concentrations over the past 60 million years. Nature 406, 695–699.

Pedro, G., 1968. Distribution des principaux types d'altération chimiques à la surface de globe. Rev. Géographie Phys. Dyn. 5, 457–470.

Phillips, S.C., Johnson, J.E., Underwood, M.B., Guo, J., Giosan, L., Rose, K., 2014. Long-timescale variation in bulk and clay mineral composition of Indian continental margin sediments in the Bay of Bengal, Arabian Sea, and Andaman Sea. Mar. Pet. Geol. 58, 117–138. doi:10.1016/j.marpetgeo.2014.06.018

Post, J.E., Burnham, C.W., 1986. Modeling tunnel-cation displacements in hollandites using structure-energy calculations. Am. Mineral. 71, 1178–1185.

Prasad, G., 1983. A review of the early Tertiary bauxite event in South America, Africa and India. J. Afr. Earth Sci. 1983 1, 305–313. doi:10.1016/S0731-7247(83)80015-9

Radhakrishna, B.P., 1993. Neogene uplift and geomorphic rejunevation of the Indian Peninsula. Curr. Sci. 64.

Ramstein, G., Khodri, M., Donnadieu, Y., Fluteau, F., Goddéris, Y., 2005. Impact of the hydrological cycle on past climate changes: three illustrations at different time scales. Comptes Rendus Geosci. 337, 125–137. doi:10.1016/j.crte.2004.10.016

Renne, P.R., Balco, G., Ludwig, K.R., Mundil, R., Min, K., 2011. Response to the comment by W.H. Schwarz et al. on "Joint determination of ^{40}K decay constants and ^{40}Ar*/^{40}K for the Fish Canyon sanidine standard, and improved accuracy for ^{40}Ar/^{39}Ar geochronology" by P.R. Renne et al. (2010). Geochim. Cosmochim. Acta 75, 5097–5100. doi:10.1016/j.gca.2011.06.021

Renne, P.R., Cassata, W.S., Morgan, L.E., 2009. The isotopic composition of atmospheric argon and ^{40}Ar/^{39}Ar geochronology: Time for a change? Quat. Geochronol. 4, 288–298. doi:10.1016/j.quageo.2009.02.015

Retallack, G.J., 2010. Lateritization and Bauxitization Events. Econ. Geol. 105, 655–667. doi:10.2113/gsecongeo.105.3.655

Riffel, S.B., Vasconcelos, P.M., Carmo, I.O., Farley, K.A., 2015. Combined ^{40}Ar/^{39}Ar and (U–Th)/He geochronological constraints on long-term landscape evolution of the Second Paraná Plateau and its ruiniform surface features, Paraná, Brazil. Geomorphology 233, 52–63. doi:10.1016/j.geomorph.2014.10.041

Roddick, J.C., Cliff, R.A., Rex, D.C., 1980. The evolution of excess argon in alpine biotites — A ^{40}Ar-^{39}Ar analysis. Earth Planet. Sci. Lett. 48, 185–208. doi:10.1016/0012-821X(80)90181-8

Rowley, D.B., Currie, B.S., 2006. Palaeo-altimetry of the late Eocene to Miocene Lunpola basin, central Tibet. Nature 439, 677–681. doi:10.1038/nature04506

Ruffet, G., Innocent, C., Michard, A., Féraud, G., Beauvais, A., Nahon, D., Hamelin, B., 1996. A geochronological $^{40}Ar^{39}Ar$ and $^{87}Rb^{81}Sr$ study of K-Mn oxides from the weathering sequence of Azul, Brazil. Geochim. Cosmochim. Acta 60, 2219–2232. doi:10.1016/0016-7037(96)00080-4

Russell, J., Chadwick, B., Rao, B.K., Vasudev, V.N., 1996. Whole-rock Pb/Pb isotopic ages of Late Archaean limestones, Karnataka, India. Precambrian Res. 78, 261–272. doi:10.1016/0301-9268(95)00082-8

Schmidt, P.W., Prasad, V., Ramam, P.K., 1983. Magnetic ages of some Indian laterites. Palaeogeogr. Palaeoclimatol. Palaeoecol. 44, 185–202. doi:10.1016/0031-0182(83)90102-5

Sun, J., Ye, J., Wu, W., Ni, X., Bi, S., Zhang, Z., Liu, W., Meng, J., 2010. Late Oligocene-Miocene mid-latitude aridification and wind patterns in the Asian interior. Geology 38, 515–518. doi:10.1130/G30776.1

Tardy, Y., 1997. Petrology of laterites and tropical soils. Balkema, Rotterdam, Netherlands, pp. 408.

Tardy, Y., Roquin, C., 1998. Dérive des continents paleoclimats et altérations tropicales. BRGM, Orléan, France, pp. 484.

Thomas, M.F., 1994. Geomorphology in the tropics: a study of weathering and denudation in low latitudes. John Wiley & Sons, Chichester, UK, pp. 482.

Turner, G., Cadogan, P.H., 1974. Possible effects of ^{39}Ar recoil in ^{40}Ar-^{39}Ar dating. Proc. Fifth Lunar Sci. Conf. 2, 1601 – 1615.

Turner, S., Buseck, P.R., 1979. Manganese Oxide Tunnel Structures and Their Intergrowths. Science 203, 456–458. doi:10.1126/science.203.4379.456

Valeton, I., 1999. Saprolite-bauxite facies of ferralitic duricrust on paleosurfaces off former Pangaea. Spec. Publ. Int. Assoc. Sedimentol. 153–158.

Van der Voo, R., Spakman, W., Bijwaard, H., 1999. Tethyan subducted slabs under India. Earth Planet. Sci. Lett. 171, 7–20. doi:10.1016/S0012-821X(99)00131-4

Vasconcelos, P.M., 1999a. ^{40}Ar/^{39}Ar Geochronology of Supergene Processes in Ore Deposits. In: Lambert, David D. and Ruiz, Joaquin (Eds.), Application of Radiogenic Isotopes to Ore Deposit Research and Exploration. Reviews in Economic Geology. Society of Economic Geologists, Boulder, CO, USA, pp. 73-113.

Vasconcelos, P.M., 1999b. K-Ar and ^{40}Ar/^{39}Ar geochronology of weathering processes. Annu. Rev. Earth Planet. Sci. 27, 183–229. doi:10.1146/annurev.earth.27.1.183

Vasconcelos, P.M., Becker, T.A., Renne, P.R., Brimhall, G.H., 1992. Age and duration of weathering by ^{40}K-^{40}Ar and ^{40}Ar-^{39}Ar analysis of supergene potassium-manganese oxides. Science 258, 451–455. doi:10.1126/science.258.5081.451

Vasconcelos, P.M., Conroy, M., 2003. Geochronology of weathering and landscape evolution, Dugald River valley, NW Queensland, Australia. Geochim. Cosmochim. Acta 67, 2913–2930. doi:10.1016/S0016-7037(02)01372-8

Vasconcelos, P.M., Heim, J.A., Farley, K.A., Monteiro, H., Waltenberg, K., 2013. ^{40}Ar/^{39}Ar and (U-Th)/He - ^{4}He/^{3}He geochronology of landscape evolution and channel iron deposit genesis at Lynn Peak, Western Australia. Geochim. Cosmochim. Acta 117, 283–312. doi:10.1016/j.gca.2013.03.037

Vasconcelos, P.M., Renne, P.R., Becker, T.A., Wenk, H.-R., 1995. Mechanisms and kinetics of atmospheric, radiogenic, and nucleogenic argon release from cryptomelane during ^{40}Ar^{39}Ar analysis. Geochim. Cosmochim. Acta 59, 2057–2070. doi:10.1016/0016-7037(95)00126-3

Vasconcelos, P.M., Renne, P.R., Brimhall, G.H., Becker, T.A., 1994. Direct dating of weathering phenomena by ^{40}Ar/^{39}Ar and K-Ar analysis of supergene K-Mn oxides. Geochim. Cosmochim. Acta 58, 1635–1665. doi:10.1016/0016-7037(94)90565-7

Widdowson, M., 1997. Tertiary paleosurfaces of the SW Deccan, Western India: implication for passive margin uplift. In: Widdowson, M. (Ed.), Palaeosurfaces: Recognition, Reconstruction and Palaeoenvironmental Interpretation. Geological Society Special Publication, London, UK, pp. 221–248.

Widdowson, M., Cox, K.G., 1996. Uplift and erosional history of the Deccan Traps, India: Evidence from laterites and drainage patterns of the Western Ghats and Konkan Coast. Earth Planet. Sci. Lett. 137, 57–69. doi:10.1016/0012-821X(95)00211-T

Widdowson, M., Gunnell, Y., 1999. Tertiary palaeosurfaces and lateritization of the coastal lowlands of western peninsula India. In: Thiry, M., Simon-Coinçon, R. (Eds.), Palaeoweathering, Palaeosurfaces and Related Continental Deposits. International Association of Sedimentologists, Special Publication, Blackwell Science, Oxford, UK, pp. 245–274.

Zachos, J.C., Dickens, G.R., Zeebe, R.E., 2008. An early Cenozoic perspective on greenhouse warming and carbon-cycle dynamics. Nature 451, 279–283. doi:10.1038/nature06588

Zachos, J.C., Pagani, M., Sloan, L., Thomas, E., Billups, K., 2001. Trends, Rhythms, and Aberrations in Global Climate 65 Ma to Present. Science 292, 686–693. doi:10.1126/science.1059412

Zhisheng, A., Kutzbach, J.E., Prell, W.L., Porter, S.C., 2001. Evolution of Asian monsoons and phased uplift of the Himalaya–Tibetan plateau since Late Miocene times. Nature 411, 62 – 66. doi:10.1038/35075035

Zhu, B., Kidd, W.S.F., Rowley, D.B., Currie, B.S., Shafique, N., 2005. Age of Initiation of the India-Asia Collision in the East-Central Himalaya. J. Geol. 113, 265 – 285. doi:10.1086/428805

Figures and table caption

Figure 1. Simplified geological map (adapted from Chardon et al., 2008) superimposed to Gtopo 30 m showing the location of the Mn ore deposit pits (stars). Kappataswamy pit (Star 1); Channanghi KMK-East pit (star 2); Triveni pit (star 3); Kumsi pit (star 4); Caurem pit (star 5); Naveli 1 & 2 pits (star 6); Cudnem pit (star 7). Offshore bathymetry is from ETOPO1 (1.8 km).

Figure 2. Synthetic topographic sections with major lateritic weathering surface relics. **(a) (b)** sections located located in the figure 1. **(c)** Detailed section across the lowland pediment. The stars and numbers are the sampled open pits located in the figure 1.

Figure 3. Sampled lateritic weathering profiles. **(a)** Kappataswamy, **(b)** Channanghi KMK-E, **(c)** Triveni, **(d)** Kumsi, **(e)** Cudnem, **(f)** Caurem and **(g)** Naveli 1. White crosses show the sampling spots. (See table 1 for GPS locations and ore sample types)

Figure 4. Synthetic sketch of the different steps of preparation, observation, sub-sampling and characterization of cryptomelane grains before the isotopic dating.

Figure 5. Reflected-light photomicrographs of polished thin sections from samples collected in Sandur **(a-b)** Shimoga **(c-d)** and Goa pits **(e-f-g)**, showing cryptomelane (C), pyrolusite (P), the protore matrix (Pr), iron oxides (Fe), lithiophorite (L) and pores (V). h) SEM image showing gibbsite crystals over cryptomelane needles. See the table 1 for samples description.

Figure 6. Procedure to separate cryptomelane grain aliquots from two sample slabs **(a-b)** of the Sandur profile using from left to right the thin section, μ-XRF mapping (yellow rectangle on section) and reflected-light photomicrography (pink rectangle on section). The μ-XRF map yields the composite colored image with Mn in blue, Fe in red and K in green. C = Cryptomelane; P = Pyrolusite; G = Goethite; H = Hematite. See the table 1 for samples description

Figure 7. Electron probe microanalyses of cryptomelane on polished thin sections. The three poles of the ternary diagram are initially Mn, 10 K and 10 Al. The black, grey and

white diamonds are samples from Sandur, Shimoga and Goa, respectively. See also the data repository table DR1.

Figure 8. $^{40}Ar/^{39}Ar$ age spectra of cryptomelane grains showing regular ages, with K/Ca (black) and Ar* (grey) step curves (left), and inverse isochron diagrams (right). **(a)** Plateau age for Sandur's cryptomelane grain; **(b)** plateau age for Shimoga's cryptomelane grain with small characteristic $^{40}Ar^*$ losses from less retentive and poorly crystalline sites at the first step heating; **(c)** Forced-plateau age for Shimoga's sample grain including four apparent ages forming a reasonably flat segment; **(d)** Concordant pseudoplateaus ages for Sandur's cryptomelane grain included in the 2σ interval. MSWD = mean square weighted deviation of the inverse isochron. See the table 1 for sample description and the data repository DR2 and DR3.

Figure 9. Disturbed $^{40}Ar/^{39}Ar$ age spectra of cryptomelane grains from Shimoga Mn ore deposits with K/Ca (black) and Ar* (grey) step curves (left), and inverse isochron diagrams (right). **(a)** Hump shape spectrum that only allows estimation of maximum and minimum ages of the mixed youngest and oldest phases, respectively. **(b)** Saddle shape spectrum resulting from mixing between several phases (supergene or hypogene) that lead to incorporation of excess $^{40}Ar^*$. **(c)** Case with an inherited hypogene contaminant. In the first steps, only the supergene phase (~ 18 Ma) releases gas, the inverse isochron diagram clearly showing the contamination with a hypogene phase enriched in $^{40}Ar^*$. See the table 1 for sample description and the data repository tables DR2 and DR3.

Figure 10. $^{40}Ar/^{39}Ar$ age spectra of cryptomelane grains from Sandur Mn ore samples. Sample ID with (F) when analyzed using a double vacuum Staudacher-type furnace coupled with VG3600 mass spectrometer. Age quality is noted (A) for best quality first order age, (B) for acceptable quality second order age, and (C) for lesser quality third order age. See the table 1 for sample description, and the data repository table DR2.

Figure 11. **(a)** $^{40}Ar/^{39}Ar$ age spectra and **(b)** inverse isochron diagrams for cryptomelane grains from Shimoga Mn ore samples. See the figure 10 for the analytical system used, age quality explanation and the table 1 for sample description. See also the data repository tables DR2 and DR3.

Figure 12. **(a)** $^{40}Ar/^{39}Ar$ age spectra and **(b)** inverse isochron diagrams for cryptomelane grains from Goa Mn ore samples. See the figure 10 for the analytical system used, age quality explanation and the table 1 for sample description. See also the data repository tables DR2 and DR3.

Figure 13. Synthesis of the $^{40}Ar/^{39}Ar$ ages results accounting for two-confidence order (A) and (B) (see text and figure 9 for explanations). **(a)** Age probability curves accounting for 1/3 of the total signal from all the validated ages weighted for the three distinct areas (N_{Sandur}=19, $N_{Shimoga}$=10 and N_{Goa}=10) enhancing the major weathering peaks that document the major weathering periods W1, W2a, and W2b (vertical colored bands). The ages are also plotted against the altitude. **(b)** Paleo-latitudinal variation of the southern boundary of the Deccan Traps across climatic zones defined by evaporation (E) and precipitation (P) after Kent and Muttoni (2008). Note the main

weathering periods derived from the $^{40}Ar/^{39}Ar$ ages in (a) also correspond to the period when peninsular India drift across the humid equatorial belt where P > E. **(c)** Global benthic $\delta^{18}O$ curve from Zachos et al. (2008) and associated global deep ocean temperature relative to actual T°C. PETM = Paleocene-Eocene Thermal Maximum; EECO = Early Eocene Climatic Optimum; MECM = Mid-Eocene Climatic Maximum; EOC = Early Oligocene Cooling; LOW = Late Oligocene Warming; MMCM = Mid-Miocene Climatic Maximum.

Table 1. Field characteristics of samples from Sandur, Shimoga and Goa Mn ore deposits (Peninsular India) and description of cryptomelane grains extracted from these samples. Other mineral species were also identified by reflected-light microscopy, XRD and SEM.

Table 2. Synthesis of the $^{40}Ar/^{39}Ar$ ages presenting the plateau ages, the inverse isochrons ages with their properties, and the integrated ages. The results in bold are considered as the preferred ages. See the figure 10 for more information about the analytical system used.

Figure 1
Click here to download high resolution image

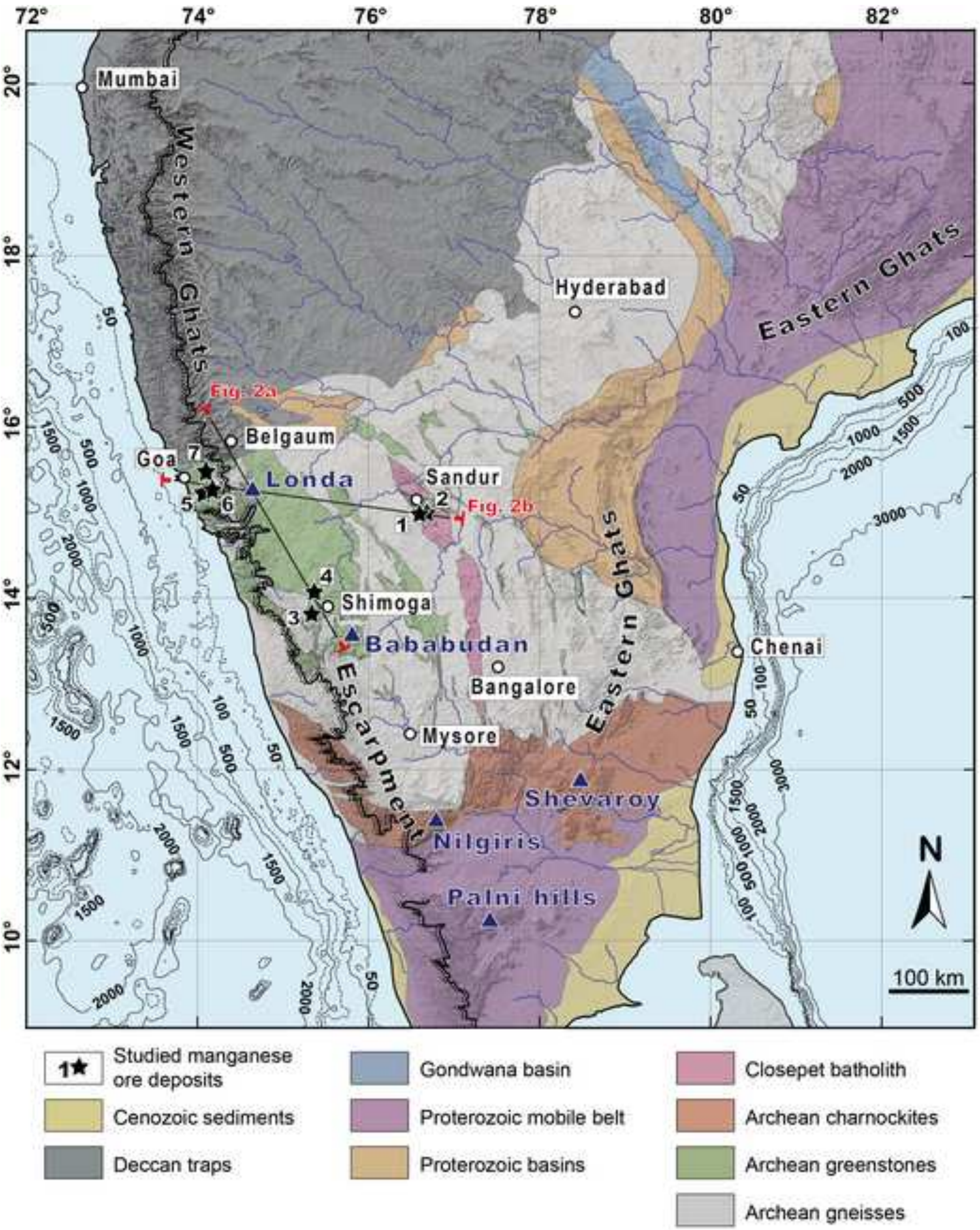

FIG. 1 (2 columns)

Figure 2

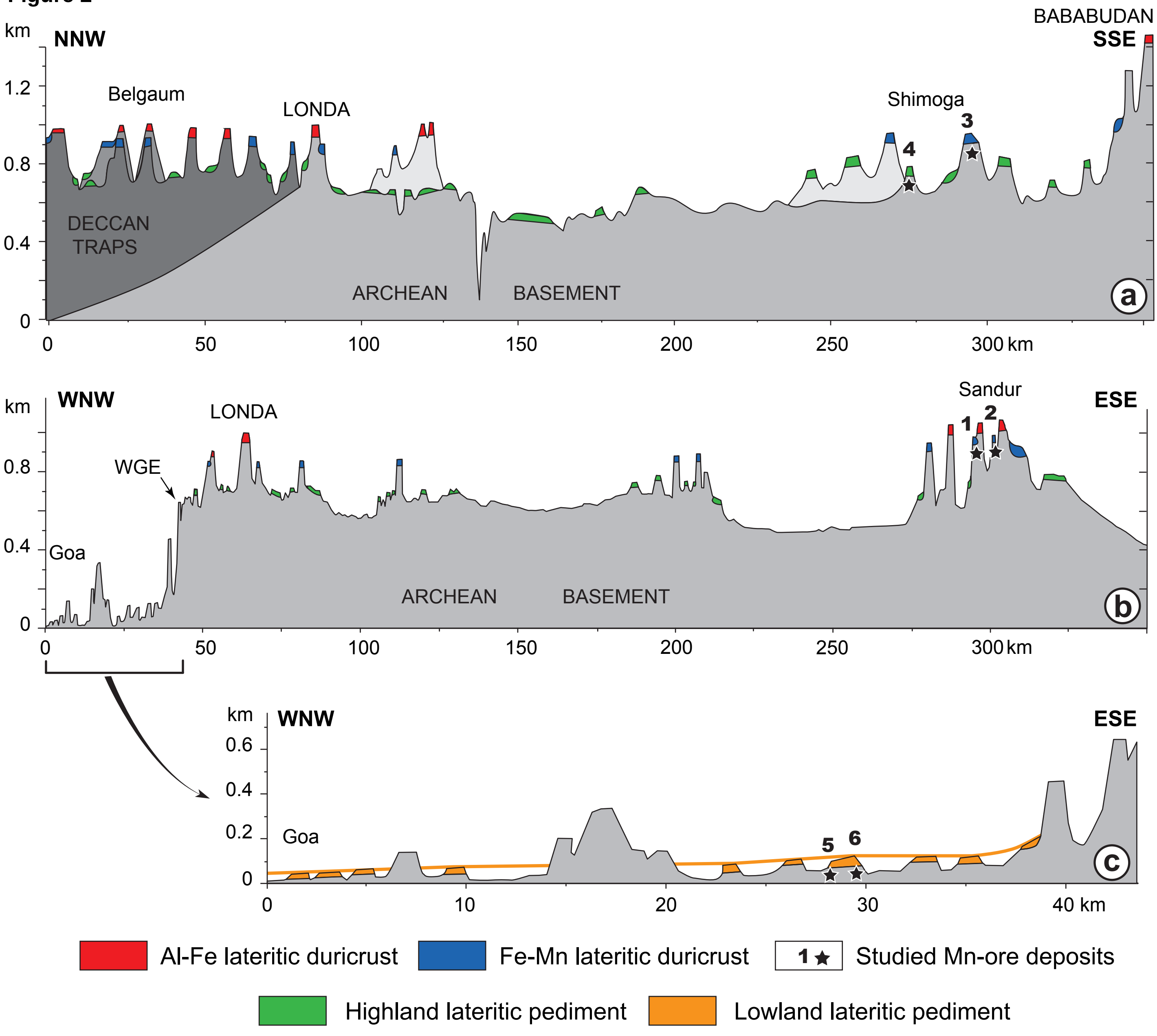

FIG.2 (2 columns)

Figure 3
Click here to download high resolution image

FIG. 3 (2 columns)

Figure 4
Click here to download high resolution image

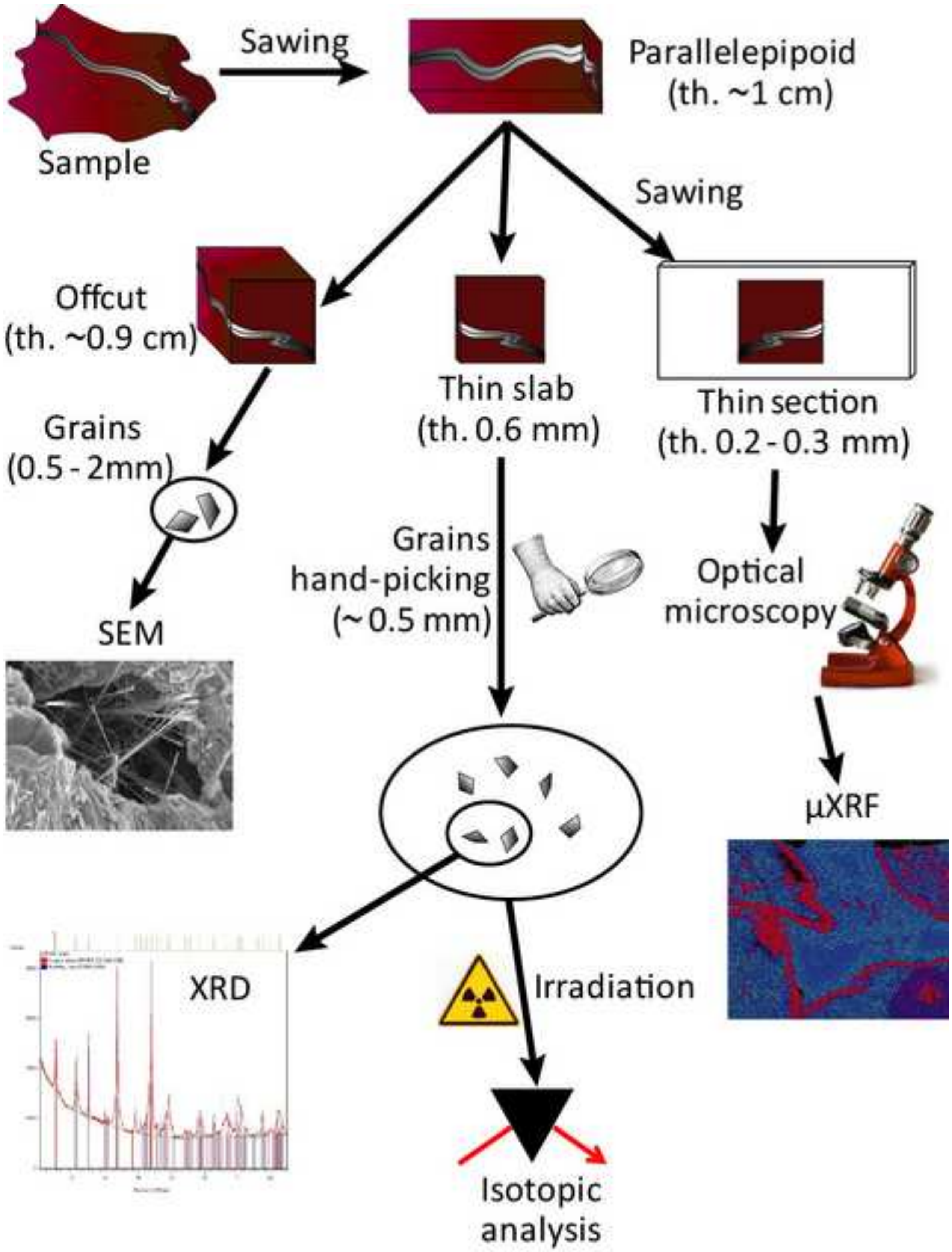

FIG. 4 (1 column)

Figure 5
Click here to download high resolution image

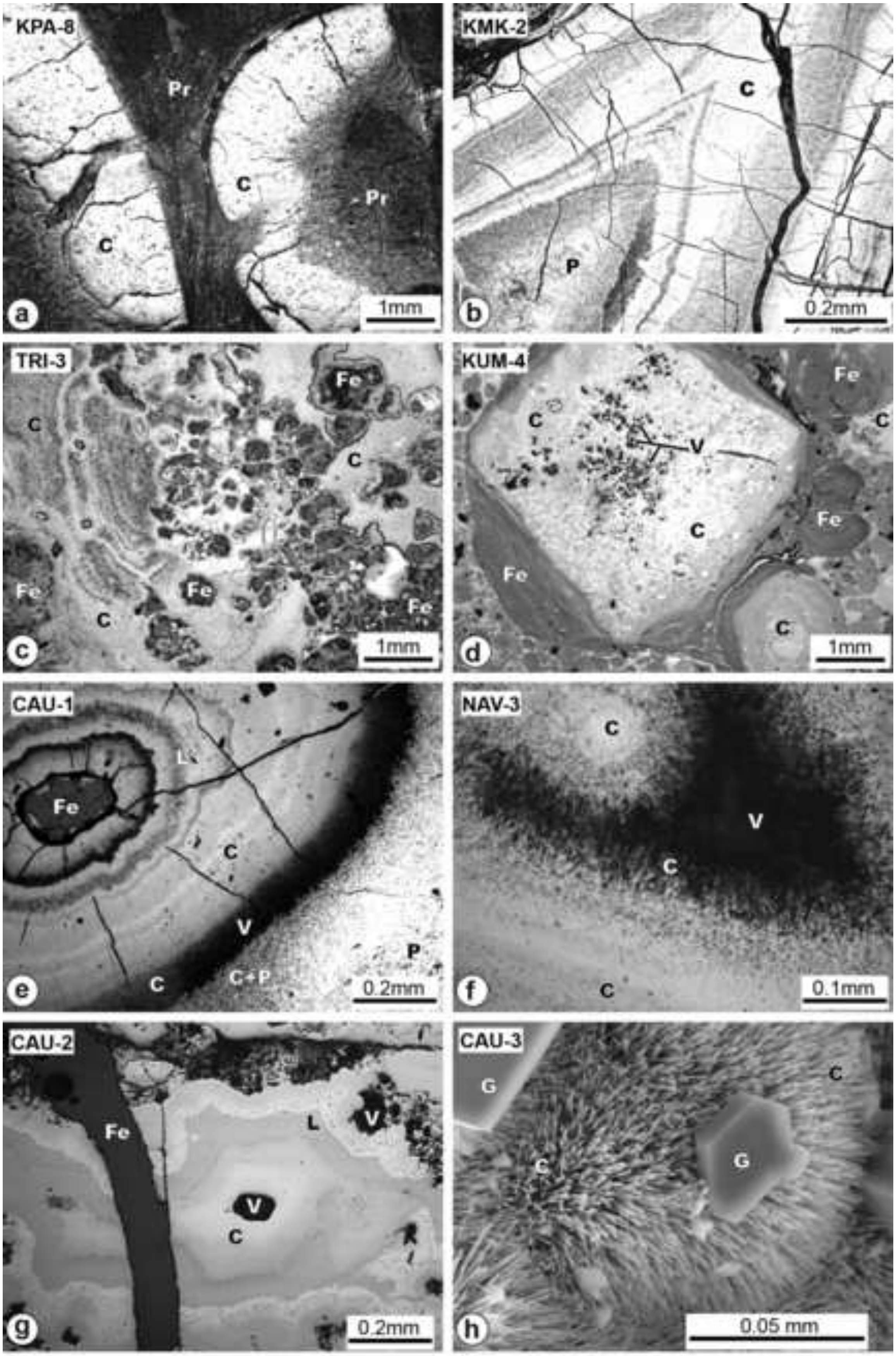

FIG. 5 (1.5 columns)

Figure 6
Click here to download high resolution image

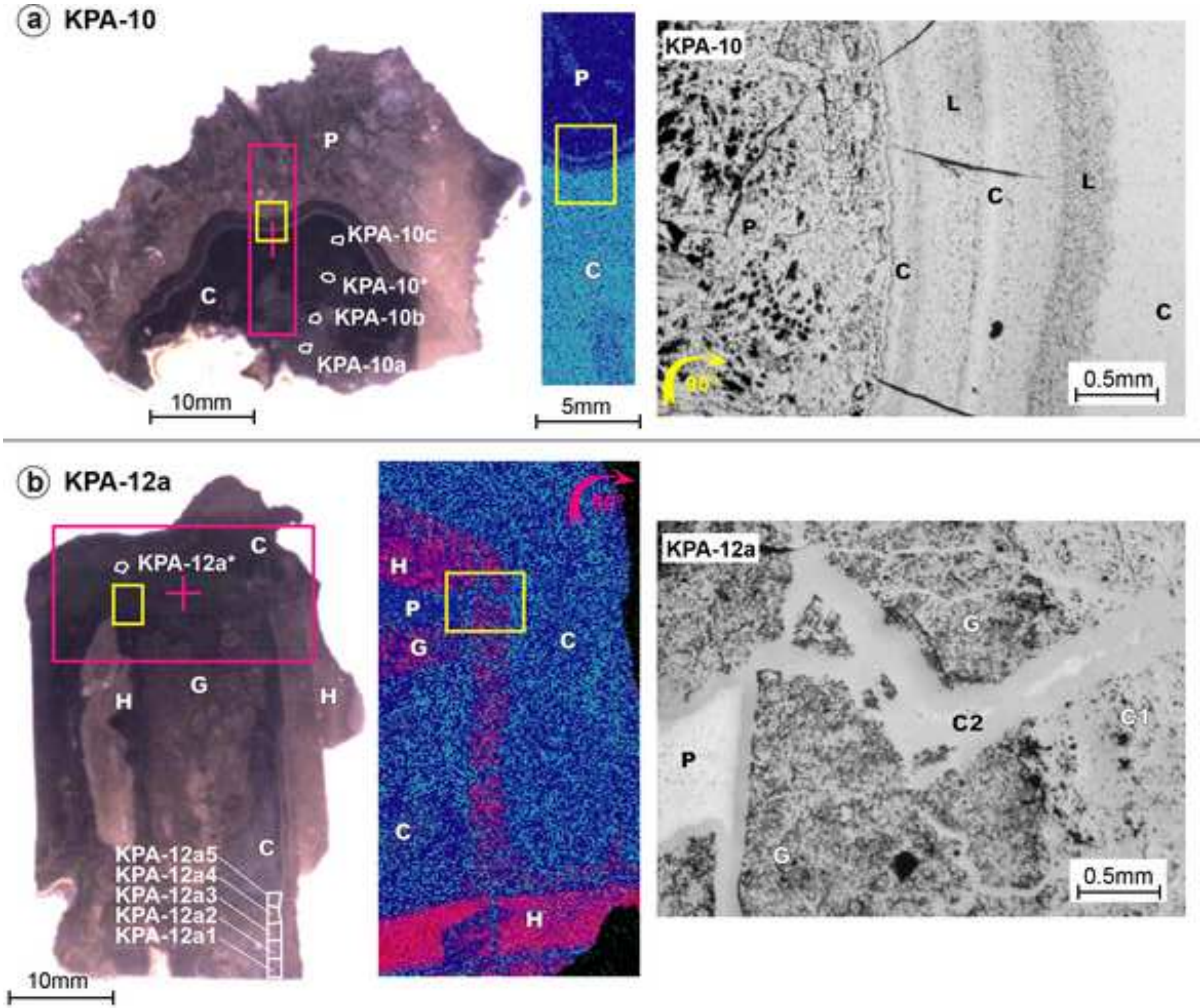

FIG. 6 (2 columns)

Figure 7
Click here to download high resolution image

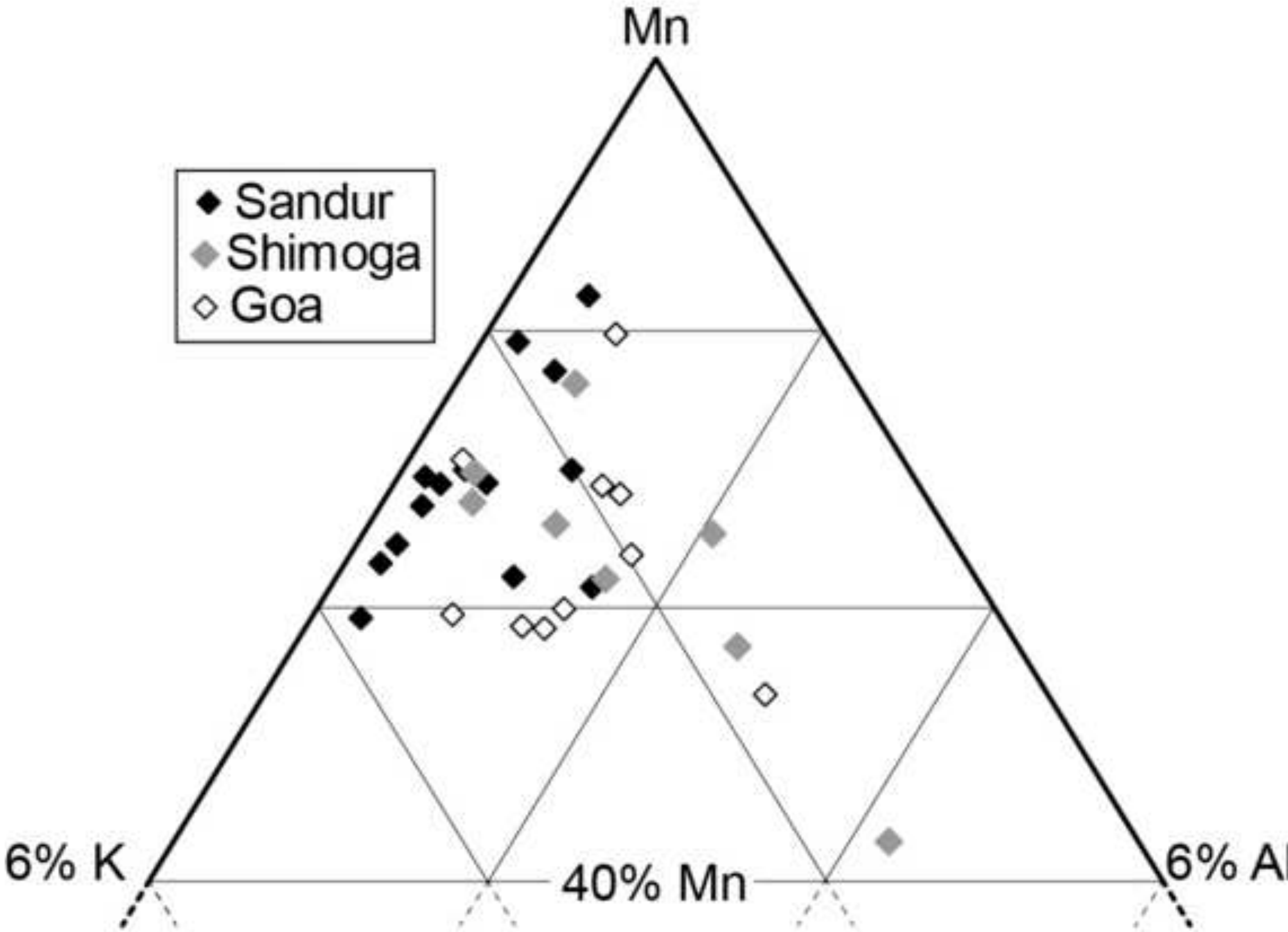

FIG. 7 (1 column)

Figure 8

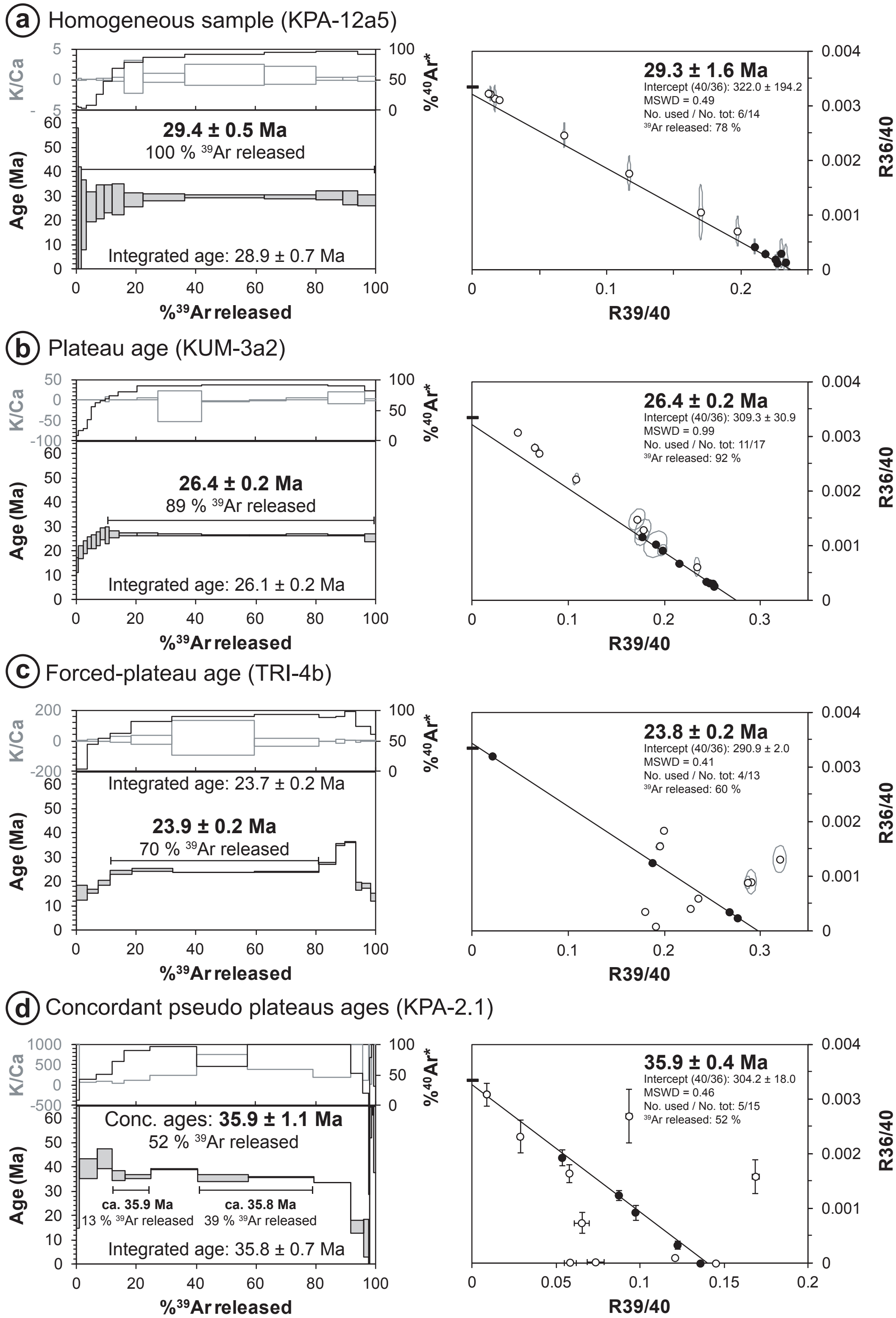

FIG. 8 (1.5 columns)

Figure 9

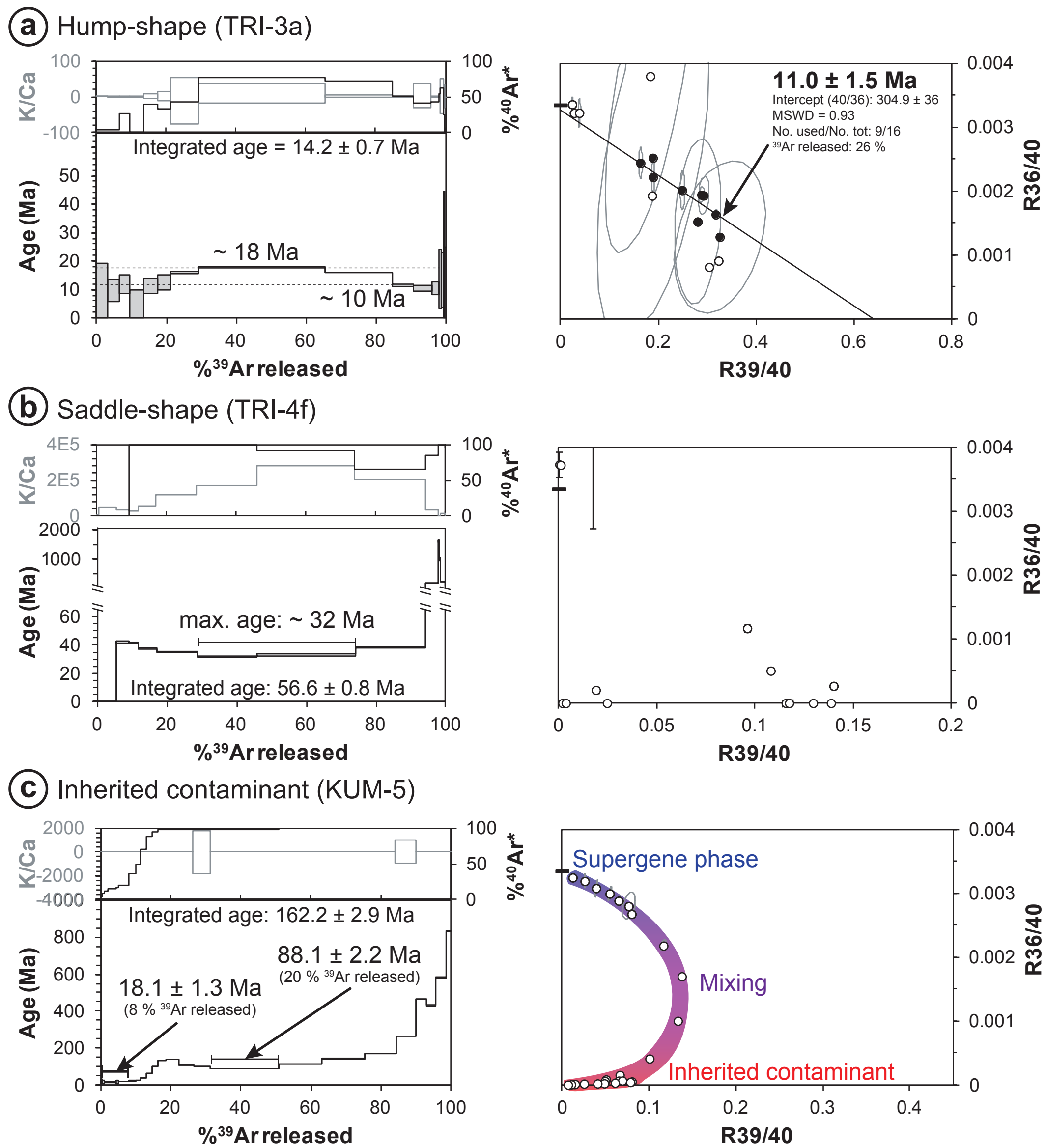

FIG. 9 (1.5 columns)

Figure 10

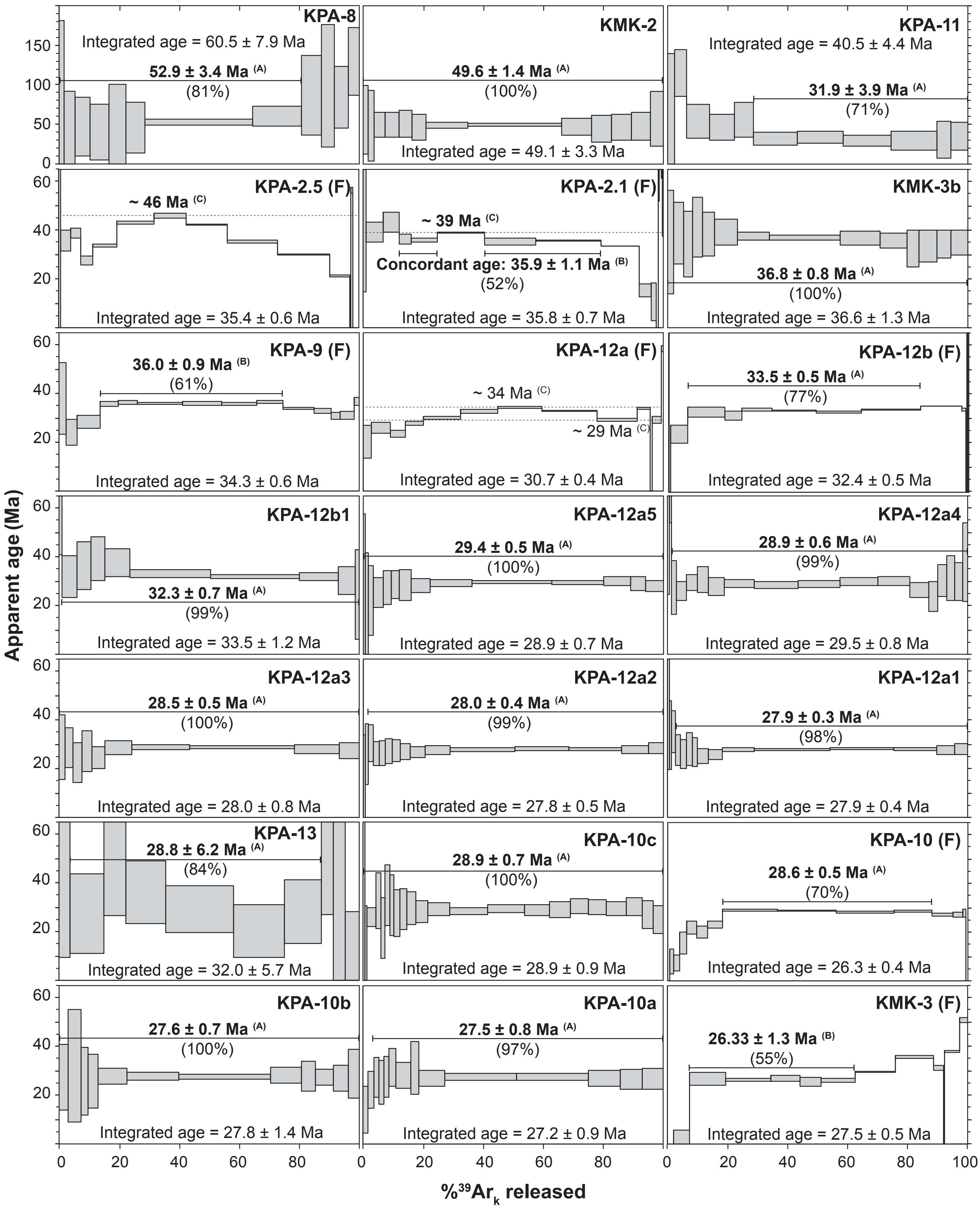

FIG. 10 (2 columns)

Figure 11

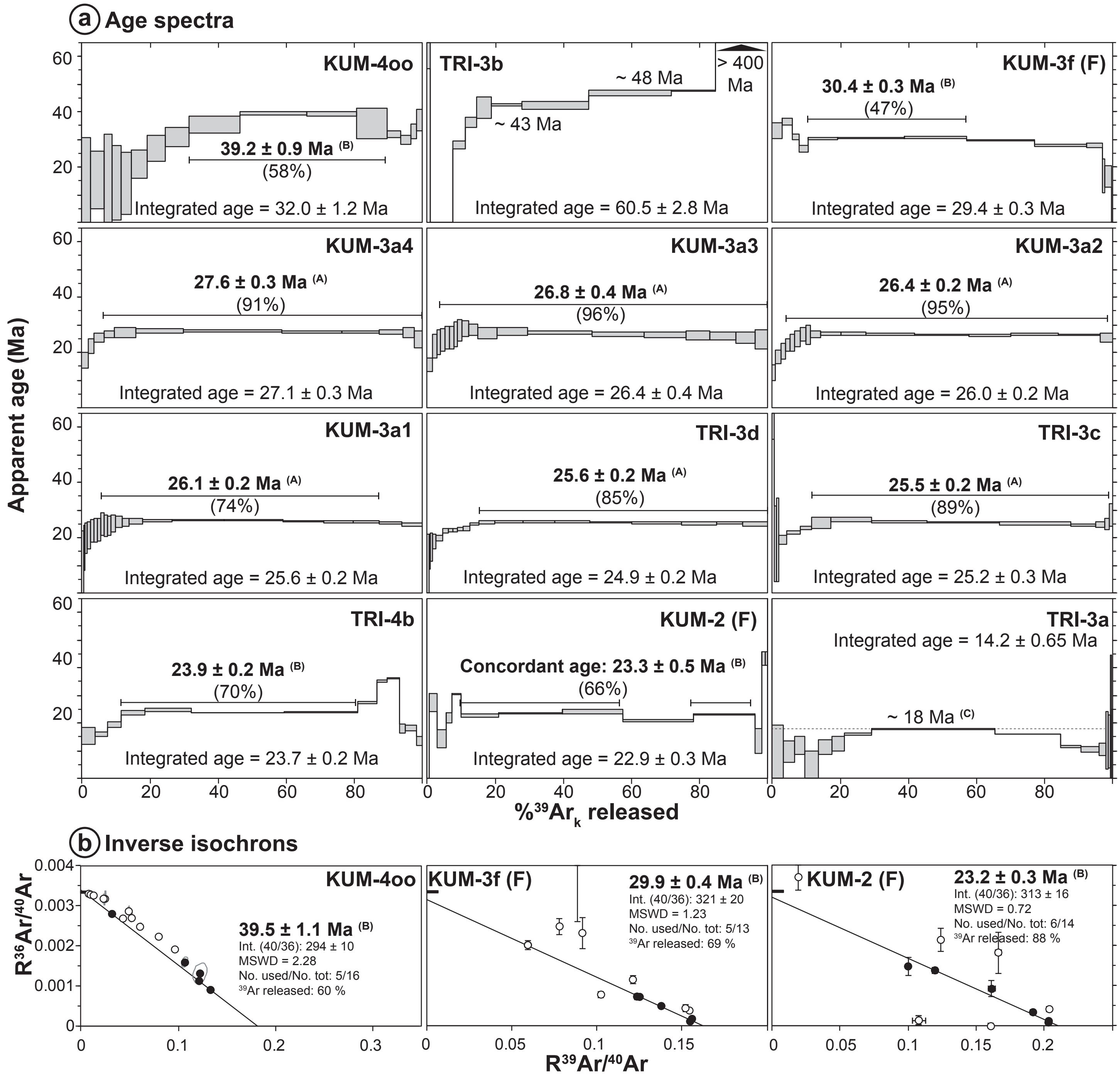

FIG. 11 (2 columns)

Figure 12

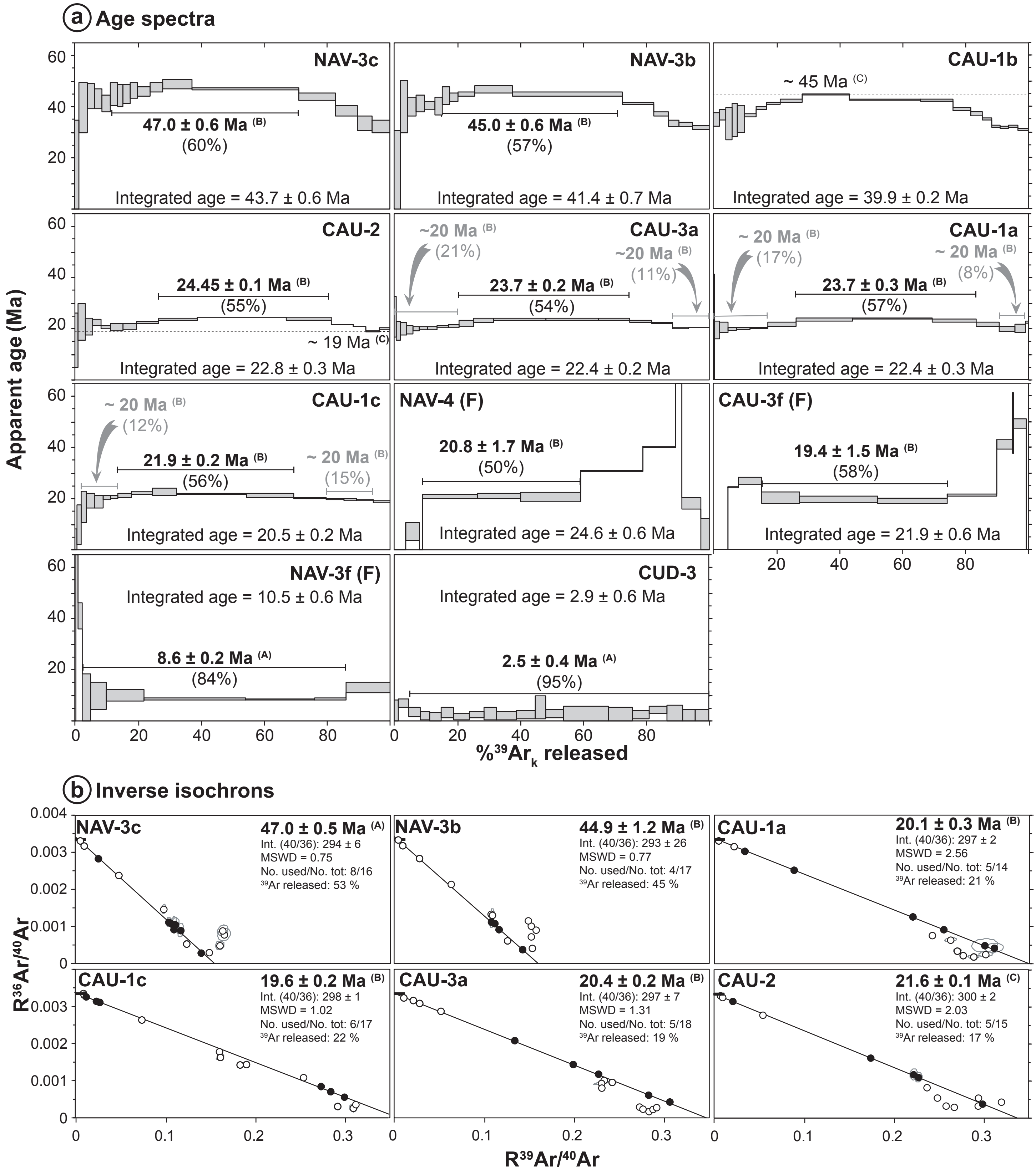

FIG. 12 (2 columns)

Figure 13

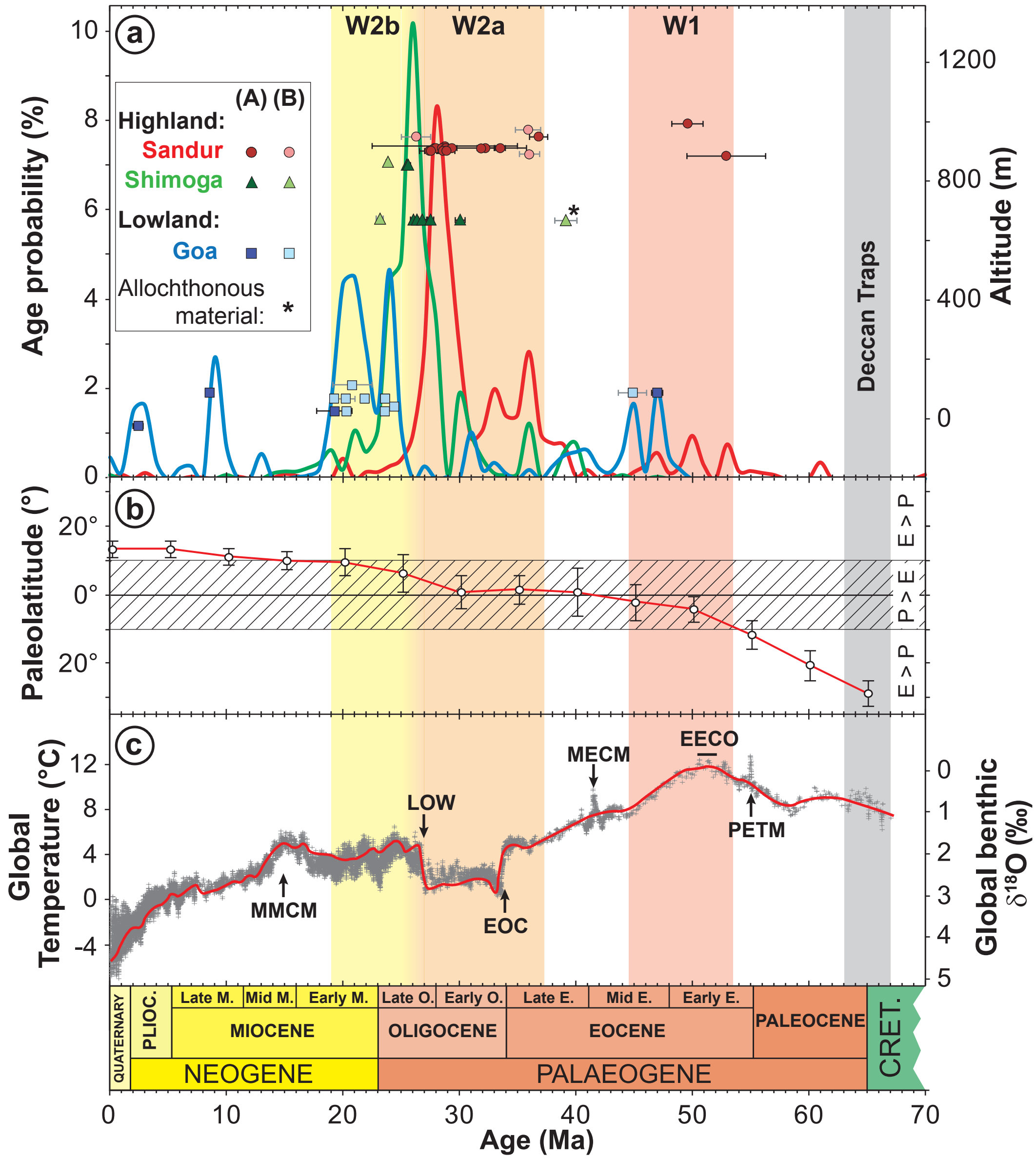

FIG. 13 (1.5 columns)

Table 1
Click here to download Table: R2_Table. 1.xlsx

Location and mine	Sample ID	Depth ± 2m	Latitude N	Longitude E	Ore type	Mineral species observed	Grains ID	Cryptomelane crystallization type
Sandur								
Kappataswamy								
	KPA-2	-140	14° 59' 59''	76° 32' 42''	Massive Mn-ore with cavities ≤ 1cm	Cryptomelane, Goethite, Nsutite, Pyrolusite	KPA-2.1	Internal band from colloidal overgrowth microstructure
							KPA-2.5	External band from colloidal overgrowth microstructure
	KPA-8	-125	15° 0' 2''	76° 32' 42''	Platy Mn-ore developed from siliceous protore	Cryptomelane, Pyrolusite, Lithiophorite	KPA-8	Botryoidal
	KPA-9	-123	15° 0' 1''	76° 32' 38''	Platy Mn-ore developed from siliceous protore	Cryptomelane, Quartz, Pyrolusite,	KPA-9	Massive cryptocrystalline domain
	KPA-10	-111	15° 0' 1''	76° 32' 38''	Massive Mn-ore with cavities > 1cm	Cryptomelane, Pyrolusite, Goethite, Hematite	KPA-10a	Internal band from geodic overgrowth microstructure
							KPA-10b	1st intermediate band from geodic overgrowth microstructure
							KPA-10	2nd intermediate band from geodic overgrowth microstructure
							KPA-10c	External band from geodic overgrowth microstructure
	KPA-11	-103	15° 0' 1''	76° 32' 38''	Platy Mn-ore developed from siliceous protore	Cryptomelane, Pyrolusite, Goethite,	KPA-11	Cryptocrystalline plasma filling a microfracture
	KPA-12a	-102	15° 0' 1''	76° 32' 38''	Platy Mn-ore with pods	Cryptomelane, Goethite, Hematite	KPA-12a	Cryptocrystalline domain filling a microfracture
							KPA-12a1	Massive cryptocrystalline domain
							KPA-12a2	Massive cryptocrystalline domain
							KPA-12a3	Massive cryptocrystalline domain
							KPA-12a4	Massive cryptocrystalline domain
							KPA-12a5	Massive cryptocrystalline domain
	KPA-12b	-102	15° 0' 1''	76° 32' 38''	Platy Mn-ore with pods	Cryptomelane, Pyrolusite	KPA-12b	Massive cryptocrystalline domain
							KPA-12b2	Massive cryptocrystalline domain
	KPA-13	-96	15° 0' 1''	76° 32' 37''	Platy Mn-ore developed from siliceous protore	Cryptomelane, Birnessite, Hematite	KPA-13	Veins of cryptocrystalline plasma
Channanghi KMK-East								
	KMK-2	-37	14° 59' 48''	76° 34' 37''	Massive Mn-ore with cavities > 1cm	Cryptomelane, Pyrolusite, Lithiophorite	KMK-2	Colloidal overgrowth microstructure
	KMK-3	-60	14° 59' 46''	76° 34' 38''	Massive Mn-ore with cavities > 1cm	Cryptomelane, Nsutite, Lithiophorite	KMK-3	External band from colloidal overgrowth microstructure
							KMK-3b	Internal band from colloidal overgrowth microstructure
Shimoga								
Triveni								
	TRI-3	-18	13° 53' 50''	75° 24' 46''	Massive developed from Banded Hematite Quartzite	Cryptomelane, Goethite, Birnessite	TRI-3a	Massive cryptocrystalline domain
							TRI-3b	Massive cryptocrystalline domain
							TRI-3c	Massive cryptocrystalline domain
							TRI-3d	Massive cryptocrystalline domain
	TRI-4	-8	13° 53' 46''	75° 24' 43''	Massive developed from Banded Hematite Quartzite	Cryptomelane, Pyrolusite, Lithiophorite	TRI-4b	Massive cryptocrystalline domain
							TRI-4f	Massive cryptocrystalline domain
Kumsi								
	KUM-2	-15	14° 6' 11''	75° 24' 15''	Massive developed from Banded Hematite Quartzite	Cryptomelane, Goethite, hematite	KUM-2	Massive cryptocrystalline domain
	KUM-3	-18	14° 6' 11''	75° 24' 14''	Massive developed from Banded Hematite Quartzite	Cryptomelane, Pyrolusite, Hematite	KUM-3a1	Massive cryptocrystalline domain
							KUM-3a2	Massive cryptocrystalline domain
							KUM-3a3	Massive cryptocrystalline domain
							KUM-3a4	Massive cryptocrystalline domain
							KUM-3f	Massive cryptocrystalline domain
	KUM-4	-20	14° 6' 10''	75° 24' 15''	Brecchia with manganiferous clasts and ferruginous oolithes	Cryptomelane, Hollandite, Hematite	KUM-4oo	Clast initially from massive cryptocrystalline domain
	KUM-5	-21	14° 6' 11''	75° 23' 55''	Massive developed from Banded Hematite Quartzite	Cryptomelane, Lithiophorite, Goethite, Kaolinite	KUM-5	Veins of cryptocrystalline plasma
Goa								
Caurem								
	CAU-1	-32	15° 7' 2''	74° 8' 40''	Clastic with ferruginous and manganiferous clasts	Cryptomelane, Pyrolusite, Goethite, Lithiophorite, Hematite	CAU-1a	Colloidal overgrowth microstructure
							CAU-1b	Colloidal overgrowth microstructure
							CAU-1c	Colloidal overgrowth microstructure
	CAU-2	-39	15° 7' 3''	74° 8' 40''	Fe-oxides with Mn-rich veins filled by percolation	Cryptomelane, Hematite, Lithiophorite, Kaolinite	CAU-2	Porous domains with visible needles
	CAU-3	-55	15° 7' 3''	74° 8' 39''	Clastic with ferruginous and manganiferous clasts	Cryptomelane, Hollandite, Goethite, Gibbsite	CAU-3a	Internal band from colloidal overgrowth microstructure
							CAU-3f	External band from colloidal overgrowth microstructure
Naveli								
	NAV-3	-56			Manganiferous lens included in saprolite	Cryptomelane, Nsutite	NAV-3b	Massive cryptocrystalline domain
							NAV-3c	Massive cryptocrystalline domain
			15° 7' 55''	74° 9' 50''			NAV-3f	Cryptocrystalline plasma filling a microfracture
	NAV-4	-27	15° 8' 7''	74° 9' 32''	Accumulation of manganese in plurimetric lenses	Cryptomelane, Goethite	NAV4	Massive cryptocrystalline domain
Cudnem								
	CUD-3	-74	15° 32' 35''	74° 2' 3''	Brecchia with manganiferous clasts and ferruginous oolithes	Cryptomelane, Hollandite, Hematite	CUD-3	Massive cryptocrystalline domain

Sample			^{39}Ar release spectrum				Inverse isochron						Integrated Age, Ma	Preferred age		
Location	ID	Alt. (m)	Age, Ma	Step(s)	%^{39}Ar	Order	Age, Ma	$40Ar/36Ar_i$	MSWD	Steps	%^{39}Ar	Order		Ma	Order	Comments
SANDUR																
2	KMK-2[2]	996	49,6 ± 1,4	1-13	100	A	49,8 ± 2,8	285 ± 201	0,11	4-10	69	B	49,1 ± 3,3	49,6 ± 1,3	A	Plateau > 70% $^{39}Ar_K$
2	KMK-3b	952	36,8 ± 0,8	1-15	100	A	36,8 ± 1,2	425 ± 643	0,62	3, 6-11	72	B	36,6 ± 1,3	36,8 ± 0,8	A	Plateau > 70% $^{39}Ar_K$
2	KMK-3 (F)[1]	952	26,3 ± 1,3	3-7	55	B	25,9 ± 0,8	305 ± 29	0,17	3-7	55	B	27,5 ± 0,5	26,3 ± 1,3	B	Plateau > 50% $^{39}Ar_K$
1	KPA-13	919	28,8 ± 6,2	2-7	84	A	27,6 ± 6,7	314 ± 293	1,19	2, 4-7	77	B	32,0 ± 5,7	28,8 ± 6,2	A	Plateau > 70% $^{39}Ar_K$
1	KPA-12b (F)[1]	913	33,5 ± 0,5	3-8	77	A	33,6 ± 0,4	292 ± 4	0,94	3-8, 10	78	C	32,4 ± 0,5	33,5 ± 0,5	A	Plateau > 70% $^{39}Ar_K$
1	KPA-12b1	913	32,3 ± 0,7	2-11	99	A	32,1 ± 0,8	343 ± 64	1,12	3-10	94	A	33,5 ± 1,2	32,3 ± 0,7	A	Plateau > 70% $^{39}Ar_K$
1	KPA-12a (F)[1]	913	34,3 ± 0,3 28,6 ± 0,9	8 5	14 6	C C	28,7 ± 0,6	336 ± 24	0,86	5-7, 10, 13	47	C	30,7 ± 0,4	34,3 ± 0,3 28,6 ± 0,9	C C	Min. of oldest Max. of youngest
1	KPA-12a1	913	27,9 ± 0,3	4-15	98	A	27,9 ± 0,3	297 ± 14	1,05	4-15	98	A	27,9 ± 0,4	27,9 ± 0,3	A	Plateau > 70% $^{39}Ar_K$
1	KPA-12a2	913	28,0 ± 0,4	3-15	99	A	28,1 ± 0,4	299 ± 8	0,70	3-6, 9, 11-13	70	A	27,8 ± 0,5	28,0 ± 0,4	A	Plateau > 70% $^{39}Ar_K$
1	KPA-12a3	913	28,5 ± 0,5	1-10	100	A	28,6 ± 0,5	292 ± 17	0,99	2-9	92	A	28,0 ± 0,8	28,5 ± 0,5	A	Plateau > 70% $^{39}Ar_K$
1	KPA-12a4	913	28,9 ± 0,6	3-18	99	A	28,9 ± 0,7	312 ± 57	1,02	5-18	94	A	29,5 ± 0,8	28,9 ± 0,6	A	Plateau > 70% $^{39}Ar_K$
1	KPA-12a5	913	29,4 ± 0,5	1-14	100	A	29,3 ± 1,6	322 ± 194	0,49	9-14	78	A	28,9 ± 0,7	29,4 ± 0,5	A	Plateau > 70% $^{39}Ar_K$
1	KPA-11v	912	31,9 ± 3,9	6-11	71	A	31,3 ± 5,3	380 ± 94	0,33	3, 5-9	75	B	40,5 ± 4,4	31,9 ± 3,9	A	Plateau > 70% $^{39}Ar_K$
1	KPA-10a	904	27,5 ± 0,8	3-14	97	A	27,6 ± 1,1	296 ± 855	0,43	4, 6-8, 10-11, 13	67	B	27,2 ± 0,9	27,5 ± 0,8	A	Plateau > 70% $^{39}Ar_K$
1	KPA-10b	904	27,6 ± 0,7	1-12	100	A	27,6 ± 0,8	299 ± 370	0,06	5-12	87	B	27,8 ± 1,4	27,6 ± 0,5	A	Plateau > 70% $^{39}Ar_K$
1	KPA-10 (F)[1]	904	28,6 ± 0,5	8-12	70	A	28,8 ± 0,6	301 ± 38	0,83	8-9, 11, 13-14	54	A	26,3 ± 0,4	28,6 ± 0,5	A	Plateau > 70% $^{39}Ar_K$
1	KPA-10c	904	28,9 ± 0,7	1-22	100	A	28,9 ± 1,1	294 ± 262	0,96	5, 10, 13-14, 17, 19, 21-22	49	A	28,9 ± 0,9	28,9 ± 0,7	A	Plateau > 70% $^{39}Ar_K$
1	KPA-9 (F)[1]	892	36,0 ± 0,9	4-9	61	B	36,2 ± 0,5	293 ± 23	0,37	4, 6, 8-9, 14	43	B	34,3 ± 0,6	36,0 ± 0,9	B	Plateau > 50% $^{39}Ar_K$
1	KPA-8[2]	887	52,9 ± 3,4	1-8	81	A	52,1 ± 4,9	339 ± 133	0,89	4-9	77	A	60,5 ± 7,9	52,9 ± 3,4	A	Plateau > 70% $^{39}Ar_K$
1	KPA-2.5 (F)[1]	875	46,0 ± 1,1 21,2 ± 0,4	7 11	11 6	C NGS	35,1 ± 0,7	299 ± 12	2,29	1-3, 5, 9	32	NGS	35,4 ± 0,6	46,0 ± 1,1	C	Min. of oldest
1	KPA-2.1 (F)[1]	875	35,9 ± 1,1 39,1 ± 0,3	4-5, 7-8 6	52 16	B C	35,9 ± 0,4	304 ± 18	0,46	4-5, 7-8, 14	52	B	35,8 ± 0,7	35,9 ± 1,1	B	Best fitted inverse isochrone
SHIMOGA																
3	TRI-4b	867	23,9 ± 0,2	4-7	70	B	23,8 ± 0,2	291 ± 2	0,41	1, 4, 6-7	60	C	23,7 ± 0,2	23,9 ± 0,2	B	Forced-plateau
3	TRI-3a	857	17,8 ± 0,2 10,4 ± 1,0	8 11-12	36 5	C C	11,0 ± 1,5	306 ± 36	0,93	3, 5-6, 10-15	26	C	14,2 ± 0,7	17,8 ± 0,2 10,4 ± 1,0	C C	Min. of oldest Max. of youngest
3	TRI-3b	857	42,6 ± 0,3	5-7	33	C	42,6 ± 2,0	297 ± 232	0,36	5-7	33	NGS	60,5 ± 2,8	42,6 ± 0,3	C	Max. age
3	TRI-3c	857	25,5 ± 0,2	7-14	89	A	25,5 ± 0,5	353 ± 100	1,01	7-10, 14	57	A	25,2 ± 0,3	25,5 ± 0,2	A	Plateau > 70% $^{39}Ar_K$
3	TRI-3d	857	25,7 ± 0,2	12-20	87	A	25,5 ± 0,4	281 ± 89	1,86	11-12, 15-20	70	B	24,9 ± 0,2	25,7 ± 0,2	A	Plateau > 70% $^{39}Ar_K$
4	KUM-2 (F)	675	23,3 ± 0,5	6-8, 10	66	B	23,3 ± 0,3	307 ± 16	0,65	4, 6-8, 10	67	B	22,9 ± 0,3	23,2 ± 0,3	B	Best fitted inverse isochrone
4	KUM-3a1	672	26,1 ± 0,2	8-20	74	A	25,2 ± 0,7	296 ± 17	0,92	6-14, 22	20	B	25,6 ± 0,2	26,1 ± 0,2	A	Plateau > 70% $^{39}Ar_K$
4	KUM-3a2	672	26,4 ± 0,2	5-17	95	A	26,4 ± 0,3	303 ± 28	1,02	7-16	93	A	26,0 ± 0,2	26,4 ± 0,2	A	Plateau > 70% $^{39}Ar_K$
4	KUM-3a3	672	26,8 ± 0,4	4-19	96	A	26,9 ± 0,5	294 ± 18	1,11	3-19	97	A	26,4 ± 0,4	26,9 ± 0,4	A	Plateau > 70% $^{39}Ar_K$
4	KUM-3a4	672	27,6 ± 0,3	4-11	91	A	27,7 ± 0,5	293 ± 36	0,94	5-9	78	A	27,1 ± 0,3	27,6 ± 0,3	A	Plateau > 70% $^{39}Ar_K$
4	KUM-3f (F)	672	30,4 ± 0,4	5-7	47	NGS	29,9 ± 0,4	321 ± 20	1,23	3, 5-8	69	NGS	29,4 ± 0,3	None		$^{40}Ar^*$ recoil
4	KUM-4oo	670	39,2 ± 0,9 24,0 ± 3,0	9-12 1-7	58 24	B C	40,1 ± 4,4 26,6 ± 5,3	284 ± 79 293 ± 6	1,56 1,37	10-12 4-7	43 16	B C	32,0 ± 1,2	39,2 ± 0,9	B	Forced-plateau
GOA																
6	NAV-4 (F)[2]	113	20,8 ± 1,7	6-8	54	B	20,7 ± 0,9	296 ± 25	0,41	4, 6-8, 13	56	B	24,6 ± 0,6	20,8 ± 1,7	B	Plateau > 50% $^{39}Ar_K$
6	NAV-3b[2]	88	45,0 ± 0,7	7-11	57	B	44,9 ± 1,2	293 ± 26	0,77	7-9, 11	45	B	41,4 ± 0,7	44,9 ± 1,2	B	Plateau > 50% $^{39}Ar_K$
6	NAV-3c[2]	88	47,0 ± 0,6	6-13	60	B	47,0 ± 0,5	294 ± 6	0,75	3, 6-11, 13	53	A	43,7 ± 0,6	47,0 ± 0,5	A	Best fitted inverse isochrone
6	NAV-3f (F)[2]	88	8,6 ± 0,2	4-9	84	A	8,6 ± 0,6	309 ± 94	0,55	4-9	84	B	10,5 ± 0,6	8,6 ± 0,2	A	Plateau > 70% $^{39}Ar_K$
5	CAU-1a[2]	68	23,7 ± 0,3 20,1 ± 0,2	8-10 1-6, 12-13	57 26	B B	23,7 ± 0,3 20,3 ± 0,8	293 ± 3 293 ± 25	1,99 0,45	3, 8-10 5-6, 12	59 15	C B	22,4 ± 0,3	23,7 ± 0,3 20,3 ± 0,8	B B	Plateau > 50% $^{39}Ar_K$ Concordant pseudo-plateaus
5	CAU-1b	68	44,7 ± 0,2 31,2 ± 0,4	10 19	15 15	C C	35,2 ± 0,8	294 ± 42	0,81	3-6, 15	13	NGS	39,9 ± 0,2	44,7 ± 0,2 31,2 ± 0,4	C C	Min. of oldest Max. of youngest
5	CAU-1c[2]	68	21,9 ± 0,2 19,7 ± 0,2	8-12 3-7, 14-16	57 27	B B	22,0 ± 0,3 19,6 ± 0,2	299 ± 11 298 ± 1	1,77 1,02	8-11 3-5, 14-16	41 22	B B	20,5 ± 0,3	21,9 ± 0,2 19,3 ± 0,2	B B	Plateau > 50% $^{39}Ar_K$ Concordant pseudo-plateaus
5	CAU-2	41	24,5 ± 0,1 19,2 ± 0,2	9-11 13	55 4	B C	24,0 ± 0,2 21,6 ± 0,1	294 ± 3 297 ± 2	0,92 2,56	4, 9, 11 3, 5-7, 12	29 21	NGS C	22,8 ± 0,3	24,5 ± 0,1 20,2 ± 0,3	B C	Forced-plateau Max. of youngest
5	CAU-3a[2]	25	23,7 ± 0,2 20,4 ± 0,2	10-14 1-8, 17-18	54 29	B B	23,7 ± 0,2 20,4 ± 0,2	292 ± 2 297 ± 7	1,82 1,31	3-4, 11-14 5-7, 17-18	49 19	C B	22,4 ± 0,2	23,7 ± 0,2 20,4 ± 0,2	B B	Plateau > 50% $^{39}Ar_K$ Concordant pseudo-plateaus
5	CAU-3f (F)[2]	25	19,4 ± 1,5	4-6	58	A	20,2 ± 0,4	284 ± 18	0,05	4-6	58	C	21,9 ± 0,6	19,4 ± 1,5	A	Plateau > 50% $^{39}Ar_K$
7	CUD-3	-24	2,5 ± 0,4	3-20	95	A	2,1 ± 0,6	305 ± 11	0,18	3-20	95	B	2,9 ± 0,6	2,5 ± 0,4	A	Plateau > 70% 39Ar_K

([1]) recalculated after Bonnet et al., 2014; ([2]) recalculated after Beauvais et al, 2016
Locations: 1 = Kappataswamy pit; 2 = Channanghi KMK-East pit; 3 Triveni Pit; 4 = Kumsi pit; 5 = Caurem pit; 6 = Naveli pits; 7 Cudnem pit (See also Fig. 1)
Refer to Fig. 1 for localities numbers
A = 1st order age; B = 2nd order age; C = 3rd order age; NGS = No Geological Significance

TABLE 2

Data Repository 1 EPMA

Data Repository 2 ArArCalc

Click here to download Background dataset for online publication only: R2_DR2.xlsx

Data Repository 3 Argon Integral